Remote Sensing of Environment 333 (2026) 115118

Contents lists available at ScienceDirect

Remote Sensing of Environment

journal homepage: www.elsevier.com/locate/rse

Estimation of intensity, footprint, and capacity of surface urban heat islands using a direction-enhanced adaptive synchronous extraction (DEASE) method

Qiquan Yang [a], Richen Ye [b,c,d], TC Chakraborty [e], Ting Hu [f,*], Yue Liu [g,*]

[a] College of Surveying & Geo-Informatics, Tongji University, Shanghai 200092, China
[b] Guangzhou Urban Planning & Design Survey Research Institute Co., Ltd, Guangzhou 510060, China
[c] Collaborative Innovation Center for Natural Resources Planning and Marine Technology of Guangzhou, Guangzhou 510060, China
[d] Guangdong Enterprise Key Laboratory for Urban Sensing, Monitoring and Early Warning, Guangzhou 510060, China
[e] Pacific Northwest National Laboratory, Richland, WA, USA
[f] School of Remote Sensing and Geomatics Engineering, Nanjing University of Information Science and Technology, Nanjing 210044, China
[g] Guangdong Provincial Key Laboratory of Remote Sensing and Geographical Information System, Guangzhou Institute of Geography, Guangdong Academy of Sciences, Guangzhou 510070, China

ARTICLE INFO

Edited by Jing M. Chen

Keywords:
SUHI effect
Indicator
Urban-rural gradients
Thermal impact
Spatiotemporal variations

ABSTRACT

The surface urban heat island (SUHI) effect, assessed through remotely sensed land surface temperature (LST), remains a focal point in urban climate research. Conventional indicators like SUHI intensity (SUHII) and footprint (SUHIF) capture peak values and spatial extent but fail to account for the cumulative thermal load—a critical dimension reflecting the total heat exposure imposed by spatially continuous warming, which directly limits a holistic assessment of ecological and societal impacts of the SUHI effect. Therefore, this study introduces an indicator termed SUHI capacity (SUHIC), designed to quantify the aggregated SUHI effect by integrating the magnitude of the warming signal across all affected areas, thereby enabling a more comprehensive evaluation of urban thermal environments. Furthermore, a direction-enhanced adaptive synchronous extraction (DEASE) method is proposed for the quantification of SUHIC. This method can dynamically identify the optimal background reference area based on the urban-rural LST gradients in various directions within the city, without relying on predefined mathematical models as previously. The results from 102 European cities first confirm that the directional variations in urban-rural LST gradients, and the DEASE method can effectively capture these distinctions for the simultaneous estimation of SUHII, SUHIF, and SUHIC. Secondly, the spatial patterns of absolute SUHIC values show strong associations with those of SUHIF ($R^2 > 0.86$), while its relative values (normalized by the area of urban) align more closely with SUHII ($R^2 > 0.64$). More importantly, SUHIC can serve as a crucial reference for assessing the urban thermal signal when SUHII and SUHIF diverge. The proposed method and framework contribute to standardizing the quantification of the SUHI effect.

1. Introduction

The process of urbanization is often accompanied by alterations in land cover and the population concentration, resulting in localized temperature increases and the formation of the urban heat island (UHI) effect (Li et al., 2023; Liu et al., 2022; Rizwan et al., 2008; Zhou et al., 2022). The UHI effect represents the most well-known local-scale impact of urbanization on climate (Wang et al., 2025). Consequently, there is a growing emphasis on conducting dedicated research aimed at better quantifying this effect and its potential impacts (Rajagopal et al., 2023; Wong et al., 2021). Remotely sensed land surface temperature (LST) has become a critical tool in quantifying the surface UHI (SUHI) effect (Voogt and Oke, 2003; Weng, 2009; Zhou et al., 2018). Its advantages, such as large-scale coverage, continuous monitoring, and cost-effectiveness, make it logistically easier for intra-urban and inter-urban assessments of the SUHI effect over traditional in-situ measurements (Chakraborty et al., 2020; Chang et al., 2023). Existing studies have extensively explored the SUHI effect, addressing various aspects

* Corresponding authors.
E-mail addresses: hutingrs@nuist.edu.cn (T. Hu), yliu_rs@whu.edu.cn (Y. Liu).

https://doi.org/10.1016/j.rse.2025.115118
Received 25 May 2025; Received in revised form 15 October 2025; Accepted 1 November 2025
Available online 8 November 2025

including quantitative methods, spatiotemporal variations, driving factors, and potential impacts (Chang et al., 2025; Guo et al., 2025; Li et al., 2018; Si et al., 2022; Yao et al., 2018; Zhou et al., 2018).

The SUHI intensity (SUHII) and the SUHI footprint (SUHIF) are two widely recognized and commonly used quantitative indicators for evaluating the city-scale heat island effects (Yang et al., 2023b; Zhou et al., 2018). The SUHII indicator is typically calculated as the average LST difference between the urban area and its background reference area (BRA), offering insights into the magnitude of the SUHI effect within the urban area (Li et al., 2022; Peng et al., 2012; Zhou et al., 2014). On the other hand, the SUHIF indicator characterizes the spatial extent or coverage of the SUHI effect, representing the maximum reach or area influenced by the effect (Yang et al., 2023a; Yang et al., 2019; Zhou et al., 2015). These two metrics together form the basis for understanding the spatial characteristics of the urban thermal environment and have been widely applied in the monitoring, assessment, and comparative studies of the SUHI effect (Yang et al., 2023b; Zhou et al., 2015).

However, the SUHII and SUHIF indicators exhibit some limitations. First, they only capture the peak value (one-dimensional) and spatial extent (two-dimensional) characteristics of the thermal field, failing to effectively reflect the continuous three-dimensional variation of the SUHI effect along the urban-rural gradient (Yao et al., 2022). Second, since the SUHII and SUHIF indicators possess distinct physical meanings and numerical manifestations, there is no inherent strong correlation between them (Yang et al., 2023b). This implies that a city with a higher SUHII does not necessarily have a larger SUHIF, and vice versa (Yang et al., 2023b; Yao et al., 2022). This decoupling, or even contradiction, between the two indicators makes it difficult to objectively compare the severity of the SUHI effect experienced by different cities (Yang et al., 2023b). For example, when comparing a city with high SUHII but small SUHIF with a city with low SUHII but large SUHIF, relying solely on either SUHII or SUHIF can lead to partial or even opposing conclusions (Fig. 1). This evaluation dilemma remains a significant practical gap in existing SUHI evaluation frameworks, directly hindering the scientific and precise allocation of cooling resources to cities most severely affected by the heat island effect (Fig. 1). Therefore, there is an urgent need to develop a composite indicator capable of integrating information from both SUHII and SUHIF, aiming to achieve a more comprehensive and systematic assessment of the SUHI effect and provide critical support for scientific decision-making.

Based on the Gaussian fitting technique, Yao et al. (2022) introduced an indicator, termed SUHI capacity (SUHIC), to capture the spatial continuity and cumulative nature of the SUHI effect. The SUHIC indicator quantifies the total thermal load in three-dimensional space by integrating the heat island intensity (i.e. SUHII) across all affected areas (i.e. SUHIF) (Fig. 1). This integration makes SUHIC a unified benchmark for inter-city comparison of SUHI severity. Hence, a key direct application of this indicator is to identify the critical cities that require prioritized allocation of cooling resources and policy interventions. Furthermore, the SUHIC-derived thermal load offers a foundation for indirect applications, including the estimation of urban cooling energy demand and the assessment of population heat exposure risks. Consequently, SUHIC represents not only a theoretical advancement but also a vital tool bridging scientific research with urban planning and climate adaptation practice.

However, the current estimation of SUHIC typically relies on the Gaussian surface fitting method (Yao et al., 2022), a predefined mathematical model that has notable limitations in practical applications. First, the Gaussian model assumes a sing-peak distribution of input LST data, which limits its applicability in some polycentric cities where LST values typically exhibit a multi-peak distribution pattern (Yang et al., 2019; Yang et al., 2023b). Second, the Gaussian model presupposes that LST follows a radially symmetric decay along the urban-rural gradient (Anniballe et al., 2014; Yang et al., 2019; Yao et al., 2022). In fact, due to spatially heterogeneous land cover and human activities, urban-rural LST patterns often demonstrate strong directional variations (Yang et al., 2023a). Incorporating directional variability is scientifically critical when quantifying the SUHI indicators.

In summary, although existing research has made considerable efforts and achievements in quantifying the SUHI effect, two major research gaps remain:

(1) SUHII and SUHIF capture only peak intensity and spatial extent, but fail to represent cumulative thermal load, limiting comprehensive assessment and objective cross-city comparisons.
(2) Existing Gaussian models assume single-peaked, symmetric LST distributions, which cannot adequately describe multi-peaked or

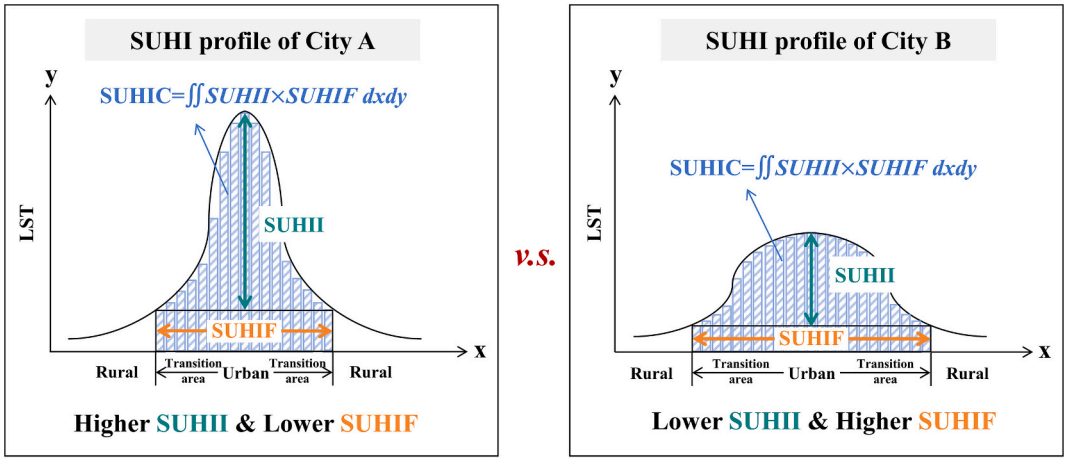

Case	SUHII	SUHIF
City A	4.0	3.2
City B	2.4	4.5

Evaluation dilemma
Which city is experiencing more severe SUHI effect?

Solution	SUHIC
City A	3.8 √
City B	3.2

Fig. 1. The conceptual diagram illustrating the definition and potential application of the SUHIC indicator. SUHII, SUHIF, and SUHIC denote the intensity, footprint, and capacity of the SUHI effect, respectively.

asymmetric urban thermal patterns, thereby limiting their broader applicability.

To address these issues, this study innovatively proposes a direction-enhanced adaptive synchronous extraction (DEASE) method, which can synchronously extract all three SUHI indicators (SUHII, SUHIF, and SUHIC) in a more flexible manner. This new method builds upon our previously proposed ASE method, which involves identifying the turning point (TP) along the urban-rural gradient where LST shifts from "rapid change" to "relative stability", thereby adaptively selecting the optimal BRA for SUHI indicator estimation (Yang et al., 2023b). The DEASE method enhances ASE by critically incorporating directional variations in LST along urban-rural gradients. Specifically, it detects TPs along multiple radial directions to derive directional SUHIF (influenced extent per direction) and directional SUHII (LST difference per direction), and then computes SUHIC by integrating the product of directional SUHII and SUHIF across all directions. In this way, without relying on restrictive assumptions about LST distributions (e.g., Gaussian models), the DEASE method facilitates the consistent and synchronous extraction of all three SUHI indicators.

Overall, the proposed DEASE method offers a unified framework for defining and estimating multiple SUHI indicators without relying on predefined mathematical models. By incorporating directional urban-rural LST variations, the DEASE method can be effectively applied to cities with complex urban thermal environments. Using this method, we quantified SUHII, SUHIF, and SUHIC across 102 European cities. The results demonstrate its strong universality and robustness, and underscore the critical importance of the SUHIC indicator for large-scale SUHI assessments and cross-city comparisons.

2. Data and study area

2.1. Data

As shown in Table 1, this study used five main datasets covering the following attributes: urban boundaries, surface temperature, water, elevation and climate zones. A detailed description of these datasets is provided below.

Considering the influence of missing data on the quantitative analyses of the SUHI effect (Lai et al., 2018; Li et al., 2022; Yang et al., 2023b), this study employed the seamless LST data produced by Zhang et al. (2022). This dataset was generated by filling the original LST observations obtained by the Moderate Resolution Imaging Spectroradiometer (MODIS) aboard the Aqua satellite. The validation results indicate that the seamless LST data exhibit good accuracy, with a global average root mean squared error below than 2 degrees Celsius (°C) (Zhang et al., 2022). This dataset has been widely utilized both globally and regionally because of its robust performance (Mashhoodi and Unceta, 2024; Yang and Zhao, 2023; Yang et al., 2023b; Yuan et al., 2023). In line with the original MODIS LST data, the seamless LST data have daily observations for both daytime (~ 13:30) and nighttime (~ 1:30), with a spatial resolution of 1 km. To facilitate analysis, the daily LST observations were seasonally and annually averaged, with June–August designated as the summer season and December–February as the winter season.

Table 1
Descriptions of data used in this study.

Type	Resolution	Period	Usage	Reference
Seamless land surface temperature (LST)	1 km	2014–2016	Estimation of SUHI indicators	Zhang et al. (2022)
Global urban boundary (GUB)	30 m	2015	Extraction of urban boundaries of selected cities and removal of the influence of surrounding urban areas	Li et al. (2020)
Global surface water (GSW)	30 m	2015	Removal of the influence of water bodies	Pekel et al. (2016)
Digital elevation model (DEM)	1 km	\	Removal of the influence of topographic reliefs	Van and Jakob (2001)
Köppen-Geiger climate classification map	1 km	\	Determination of the climate zone of cities	Beck et al. (2018)

The global urban boundary (GUB) data produced by Li et al. (2020) was used for delineating urban areas. The GUB data provide global urban polygons based on a 30-m resolution image and has been widely used in SUHI studies (Deng et al., 2024; Li et al., 2023; Liu et al., 2022; Yang et al., 2023b). The surface elevation information was sourced from the 1-km digital elevation model (DEM) produced by the Shuttle Radar Topography Mission (SRTM). This dataset was employed to mitigate the impact of topographic relief on the quantification of SUHI effect. The distribution of surface water was detected using the global surface water (GSW) data created by Pekel et al. (2016). The GSW dataset gives the annual maximum extent of global surface water at a spatial resolution of 30 m. This dataset was used for removing the influence of surface water on the SUHI indicator estimation. The climate zones were derived from the major climate classes of the Köppen–Geiger climate classification map (Beck et al., 2018). This dataset was used to identify the background climatic conditions of each city.

2.2. Study area

Building on previous studies, the GUB polygons situated within a 2 km proximity were merged into the same urban cluster (Lai et al., 2021; Yang and Zhao, 2023; Yang et al., 2023b; Zhou et al., 2014). Subsequently, a total of 102 urban clusters, varying in size and shape, were randomly selected across Europe to represent the urban areas of the target cities. We focus on European cities because they have well-documented urban development patterns and are frequently affected by severe heat waves (Shreevastava et al., 2021; García-León et al., 2021). As shown in Fig. 2, the selected 102 European cities are distributed across three climate zones: arid (7), temperate (52), and cold (43).

3. Methods

In this study, we present a novel DEASE method that enables the simultaneous estimation of SUHII, SUHIF, and SUHIC. This method began by extracting the optimal BRA in each direction based on continuous characteristics of urban-rural LST gradients. Building upon this foundation, the directional components of each SUHI indicator were computed based on their respective definitions. Ultimately, the SUHII indicators for the entire city were obtained by integrating all these directional components. In terms of implementation, the DEASE method comprises three main components: construction and division of buffers, search for turning points by directions, and calculation of SUHI indicators.

3.1. Construction and division of buffers

As shown in Fig. 3, this part consists of three main steps:

(1) Construction of buffers

For each city, we created twenty buffer rings around its urban area, with each buffer's area being half of the central urban area (Yang et al., 2023b). This design enables the outermost buffer and its inner regions to

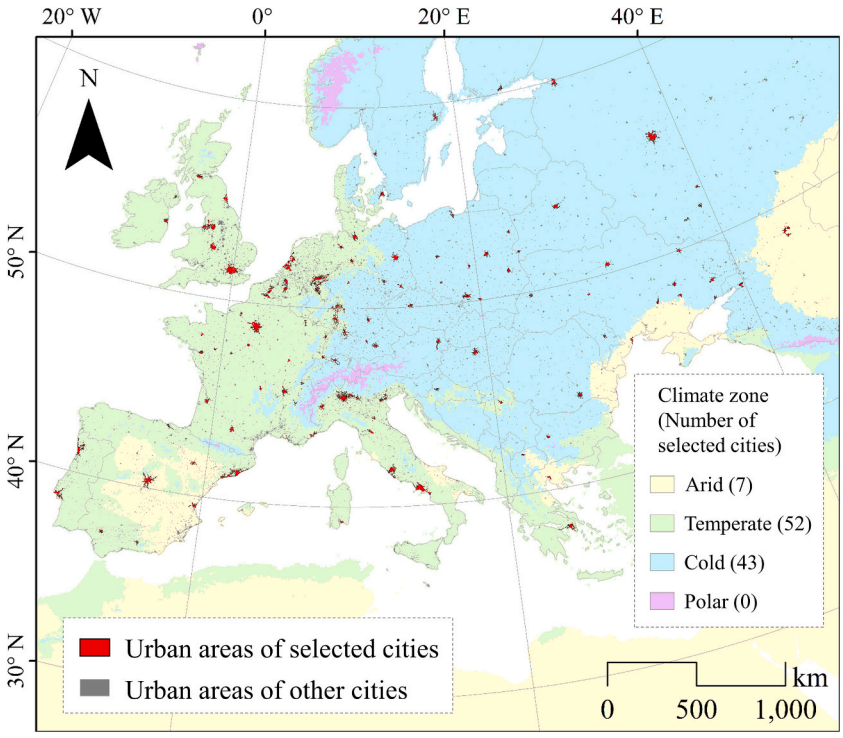

Fig. 2. The spatial distribution of 102 selected European cities and their urban areas.

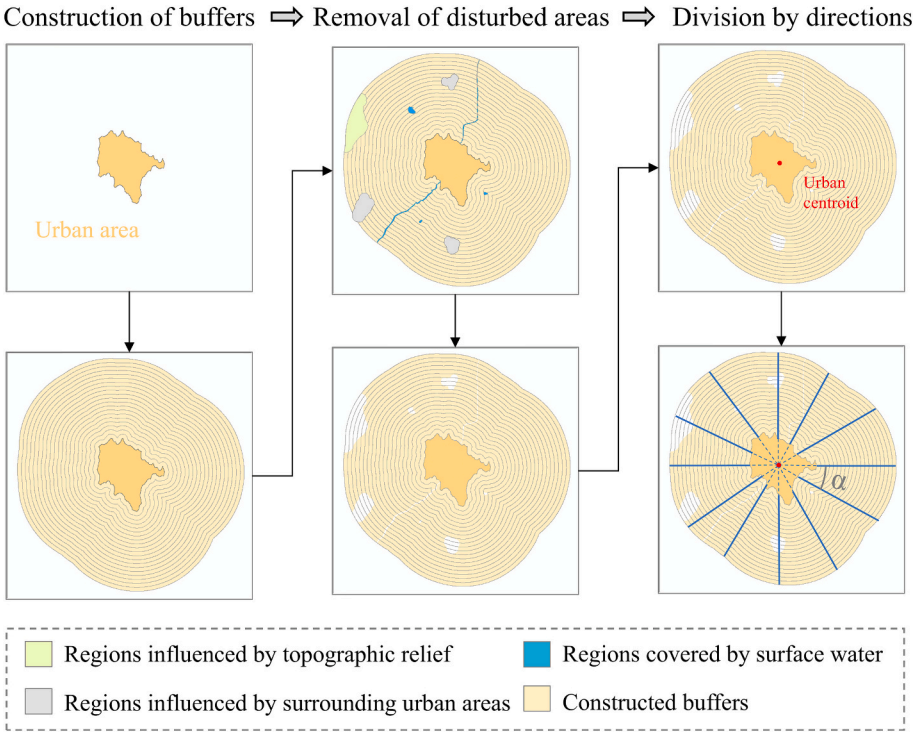

Fig. 3. The flow diagram illustrating the process of constructing and dividing buffers.

cover an area far exceeding the maximum extent influenced by the SUHI effect reported in existing studies (Yang et al., 2023b; Zhou et al., 2015). Moreover, we specified that the width of the constructed buffer rings should not be less than the spatial resolution of the LST image (1 km), ensuring that each buffer contains LST pixels. The setting of twenty buffer rings has been demonstrated to be sufficient for encompassing all turning points across the 102 European cities (see Results).

(2) Removal of disturbed areas

Adhering to established practices in previous research (Du et al., 2023; Li et al., 2022; Yang et al., 2023b; Zhou et al., 2014; Zhou et al., 2015), we excluded areas within the buffers containing water bodies and exhibiting abnormal elevation. Besides, we also removed areas within the buffers covered by other urban areas and their extensions that have

tripled in size (Yang et al., 2023b; Yao et al., 2019). The above strategies contribute to minimizing influence caused by disturbing factors, thereby enhancing the reliability of the estimated SUHI indicators (Yang et al., 2023b).

(3) Division by directions

We divided the constructed buffers equally in an angular manner, radiating outward from the center of mass of the urban area. The buffers were divided into twelve sectors at 30-degree intervals (the divisions of other angles were also attempted). Consequently, each sector consists of twenty buffer subdivisions, and their areas gradually increase in the direction away from the central urban (Fig. 3).

3.2. Search for turning points by directions

Based on previous studies (Li et al., 2019; Yang et al., 2023b), LST typically experiences an initial rapid change followed by a stabilization process when transitioning from urban to rural areas. There should be a turning point (TP) along the urban-rural LST gradients, and the regions where this TP is located represent the most optimal BRA (Yang et al., 2023b). Considering the directional differences in LST distributions, we identified TPs in various directions of the city based on the continuous characteristics of urban-rural LST gradients. In each direction, the principle of extracting the TP is depicted in Fig. 4, and the specific implementation process is as follows.

For a given city, we first calculated the mean LST within its urban area and within each buffer subdivision obtained in the previous step. Then, we employed cubic smoothing splines on the mean LSTs in different directions independently. This approach helps reduce the impact of local fluctuations on the overall pattern of urban-rural LST variations (Yang et al., 2023b). We denoted the dataset of mean LSTs in the mth direction as $\boldsymbol{T_m} = \{T_0, T_{m,1}, T_{m,2}, \ldots, T_{m,N}\}$ ($m \in \{1, 2, \ldots, M\}$), where T_0 is the mean LST of the urban area, and $T_{m,1}, T_{m,2}, \ldots, T_{m,N}$ are the smoothed mean LSTs from the *1*st to the *N*th buffer subdivision in the *m*th direction, and M and N represent the total number of directions and buffers, respectively. Next, we calculated the difference (the latter minus the former) between two neighboring elements in $\boldsymbol{T_m}$ to generate a new dataset, $\boldsymbol{\Delta T_m} = \{\Delta T_{m,1}, \Delta T_{m,2}, \ldots, \Delta T_{m,N}\}$. Obviously, according to the general patterns observed in the urban-rural LST gradients, the absolute value of the element in $\boldsymbol{\Delta T_m}$ (i.e., $|\Delta T_{m,i}|$) gradually decrease with the increase of i ($i \in \{1, 2, \ldots, N\}$) until it levels off. Thus, the TP of the mth direction can be identified by comparing $|\Delta T_{m,i}|$ with a certain threshold ΔT_t. As i gradually increases to k, and when it first satisfies the below conditions,

$|\Delta T_{m,k}| > \Delta T_t$ & $|\Delta T_{m,k+1}| \leq \Delta T_t$ (Scenarios 2&3 in Fig. 4).

or

$|\Delta T_{m,k}| > \Delta T_t$ & $|\Delta T_{m,k}| \times |\Delta T_{m,k+1}| \leq 0$ (Scenarios 1&4 in Fig. 4).

the TP of the mth direction shall be located in the kth buffer subdivision away from its urban area. Given the difference in the range and magnitude of LST variability, the threshold is defined as $\Delta T_t = Per_t \times (T_{m\_max} - T_{m\_min})$. T_{m_max} and T_{m_min} are the maximum and minimum values in $\boldsymbol{T_m}$, respectively. The scaling factor, Per_t, is set to 2 %. The rationale for choosing this value and the associated uncertainty have been extensively discussed in our earlier study (Yang et al., 2023b).

3.3. Calculation of SUHI indicators

As shown in Fig. 5, for a given city, we assumed that the area and mean LST of the urban area were S_0 and T_0, respectively. There is a total of N buffers outside the urban area, and each buffer has M subdivisions (corresponding to M directions). Suppose the area of the nth ($n \in \{1, 2, \ldots, N\}$) buffer subdivision in the mth ($m \in \{1, 2, \ldots, M\}$) direction is $S_{m,n}$ and its smoothed mean LST is $T_{m,n}$. Within this direction, the TP is situated at the position of the kth buffer subdivision ($k \in \{1, 2, \ldots, N\}$), having an area denoted as $S_{m,k}$ and an smoothed mean LST of $T_{m,k}$. Then, the computation of each SUHI indicator can be achieved as follows.

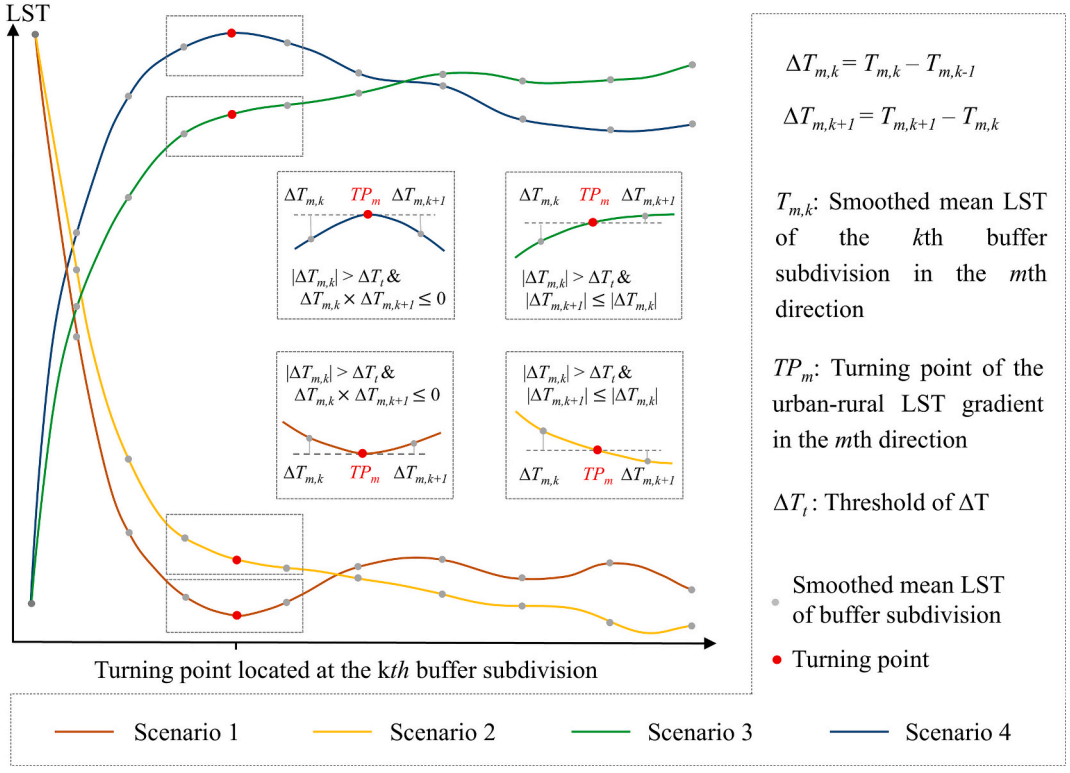

Fig. 4. A diagram illustrating the method for extracting the turning point along the urban-rural LST gradient in a specific direction. Four distinct scenarios are presented to demonstrate possible cases for locating turning points.

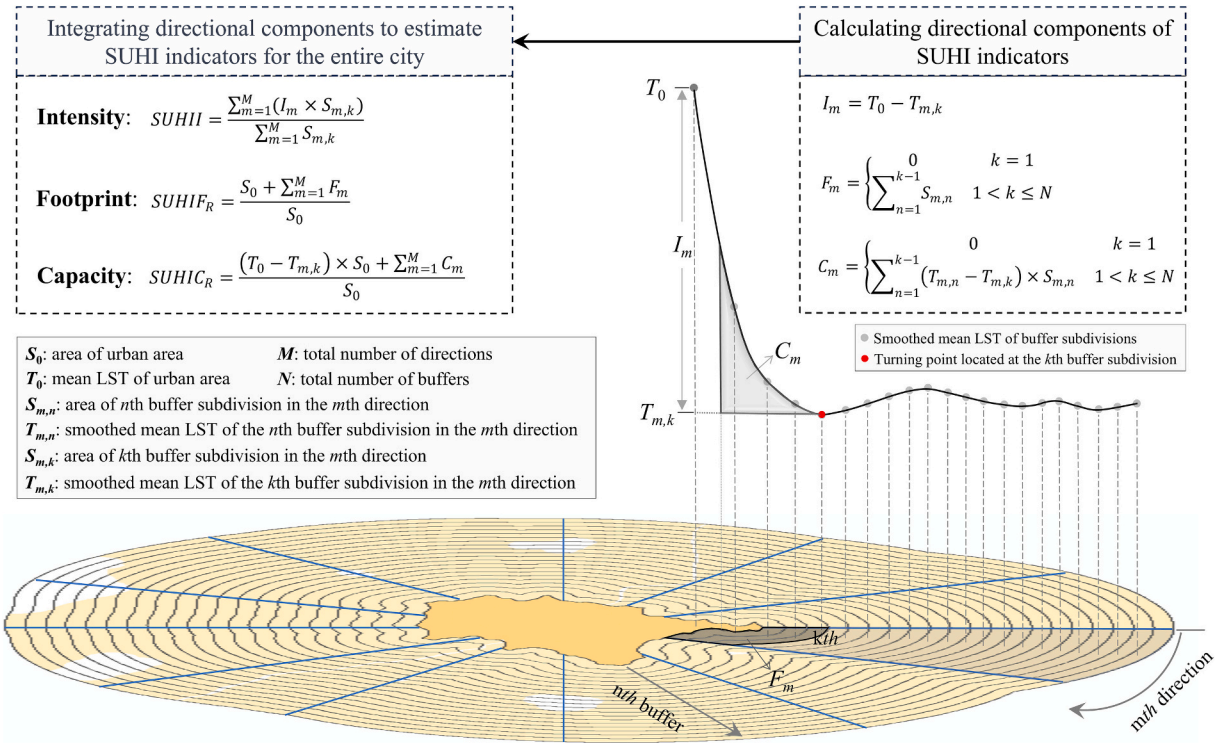

Fig. 5. Schematic representation of the direction-enhanced methodology for calculating the intensity, footprint, and capacity of the SUHI effect.

(1) SUHII

For the mth direction, the average difference in LST between the urban area and the BRA in this direction, denoted as I_m, is expressed as:

$$I_m = T_0 - T_{m,k}$$

Subsequently, the directional components are weighted and averaged using the area of the BRA as weights. This process yields the SUHII for the entire city:

$$\mathrm{SUHII} = \frac{\sum_{m=1}^{M}(I_m \times S_{m,k})}{\sum_{m=1}^{M} S_{m,k}}$$

(2) SUHIF

The area of transition regions under the influence of the SUHI effect in the mth direction, donated as F_m, can be calculated by:

$$F_m = \begin{cases} 0 & k = 1 \\ \sum_{n=1}^{k-1} S_{m,n} & 1 < k \le N \end{cases}$$

Then, the SUHIF of the entire city can be obtained by summing the areas of the urban area and transition regions for all directions:

$$\mathrm{SUHIF_A} = S_0 + \sum_{m=1}^{M} F_m$$

$\mathrm{SUHIF_A}$ represents the absolute value of the footprint, indicating the spatial extent of the SUHI effect. Considering variations in the size of the city itself, we derived the relative value of the footprint, $\mathrm{SUHIF_R}$, by normalizing the size of the urban area:

$$\mathrm{SUHIF_R} = \mathrm{SUHIF_A}/S_0$$

(3) SUHIC

The cumulative thermal load of transition regions in the mth direction, denoted as C_m, can be calculated as the following equation:

$$C_m = \begin{cases} 0 & k = 1 \\ \sum_{n=1}^{k-1} (T_{mn} - T_{mk}) \times S_{mn} & k > 1 \end{cases}$$

Then, the SUHIC for the entire city can be obtained by integrating the thermal loads in the urban area and transition regions in all directions:

$$\mathrm{SUHIC_A} = (T_0 - T_{mk}) \times S_0 + \sum_{m=1}^{M} C_m$$

$\mathrm{SUHIC_A}$ represents the absolute value of the SUHI capacity, and it is normalized by the size of the urban area to get its relative value, denoted as $\mathrm{SUHIC_R}$:

$$\mathrm{SUHIC_R} = \mathrm{SUHIC_A}/S_0$$

Note that if TP cannot be obtained in a certain direction due to missing LST data, we substitute it with the TP derived from LST gradients averaged across other available directions.

4. Results

4.1. Directional variations of urban-rural LST gradients

As depicted in Fig. 6, LST generally exhibits a pattern of rapid change along urban-rural gradients, followed by relative stability after the turning point (i.e. TP). However, there exists variation in the rate of change and the distribution pattern of LST across urban-rural gradients. This discrepancy is evident not only between different cities but also within the same city across different directions (Fig. 6a). Directional changes in urban-rural LST gradients can result in significant variations in the location of TPs and their average LSTs. Overall, the annual daytime and nighttime TPs are situated between the 1st and 14th buffer subdivisions outside of the urban area, with an average positioning around the 5th buffer subdivision (Fig. 6b). The above results underscore the directional discrepancies in the spatial distribution of the

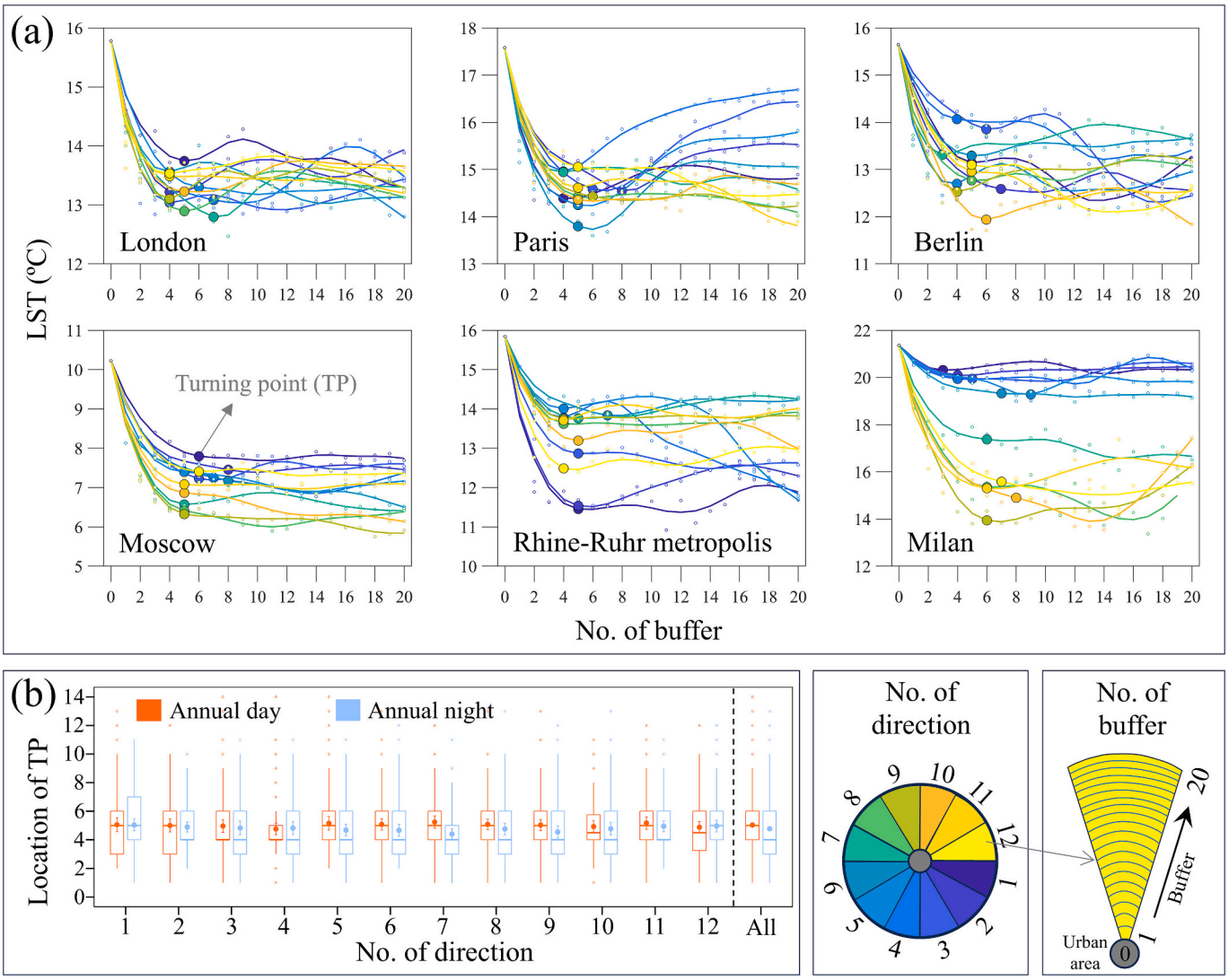

Fig. 6. Directional differences in urban-rural LST gradients and turning points. (a) An example of six typical cities. (b) Boxplots of the location of turning points in various directions across 102 European cities.

urban thermal environment and emphasize the importance of directional refinement while quantifying the SUHI effect.

4.2. Spatiotemporal discrepancies between SUHII and SUHIF

Differences between SUHII and SUHIF are evident in terms of day-night contrasts and seasonal variations. Annual daytime SUHII is predominantly concentrated in the range of 1 °C to 3 °C, with a mean value (± 95 % confidence interval) of 1.86 ± 0.16 °C, significantly ($p < 0.001$, *t*-test) higher than annual nighttime SUHII (1.14 ± 0.08 °C) (Table 2). Conversely, SUHIF exhibits comparable values between annual daytime and annual nighttime, both in absolute terms ($SUHIF_A$, 1563.3 ± 308.8 vs. 1533.8 ± 323.2 km^2, $p = 0.896$) and relative terms ($SUHIF_R$, 4.43 ± 0.28 vs. 4.13 ± 0.26, $p = 0.093$) (Table 2). In terms of seasonal variation, SUHII demonstrates a significant ($p < 0.001$) difference between summer and winter, with summertime averages over European cities nearly 2.5 times higher than those during wintertime (Table 3). Conversely, the seasonal difference in SUHIF appears to be much smaller, although it still tends to be higher in summer than in winter for European cities (Table 3). These results suggest that SUHII is more sensitive to diurnal and seasonal variations due to solar heating and urban-rural thermal contrasts, whereas SUHIF remains relatively stable because it is primarily governed by urban morphology and surface properties that remain relatively stable over time.

Spatially, annual daytime SUHII is higher in central European cities, while nighttime SUHII shows the opposite pattern (Fig. 7). This indicates pronounced daytime urban-rural thermal contrasts in these cities, driven by strong solar absorption in dense urban areas and cooling effects from surrounding vegetation, while the lower nighttime SUHII reflects more efficient urban heat release after sunset. In contrast, high SUHIF values are consistently concentrated in central European cities both day and night (Fig. 7), likely due to stable urban morphology and

Table 2
Annual daytime and nighttime averages (± 95 % confidence interval) of SUHI indicators for 102 European cities. The significance level (*p*-value) of day-night contrast is determined by *t*-tests. SUHII, SUHIF, and SUHIC denote the intensity, footprint, and capacity of the SUHI effect, respectively. The subscripts A and R indicate the absolute value and relative value of SUHI indicators, respectively.

	SUHII (°C)	$SUHIF_R$	$SUHIC_R$ (°C)	$SUHIF_A$ (km^2)	$SUHIC_A$ (°C km^2)
Annual day	1.86 ± 0.16	4.43 ± 0.28	4.53 ± 0.51	1563.3 ± 308.8	1862.9 ± 500.5
Annual night	1.14 ± 0.08	4.13 ± 0.26	2.57 ± 0.25	1533.8 ± 323.2	1046.5 ± 270.2
p-value	< 0.001	0.093	< 0.001	0.896	< 0.01

Table 3
Seasonal averages (± 95 % confidence interval) of SUHI indicators for 102 European cities. The significant level (*p*-value) of summer-winter contrast is revealed by t-tests. SUHII, SUHIF, and SUHIC denote the intensity, footprint, and capacity of the SUHI effect, respectively. The subscripts A and R indicate the absolute value and relative value of SUHI indicators, respectively.

		SUHII (°C)	$SUHIF_R$	$SUHIC_R$ (°C)	$SUHIF_A$ (km^2)	$SUHIC_A$ (°C km^2)
Day	Summer	2.89 ± 0.26	4.70 ± 0.32	7.45 ± 0.86	1634.8 ± 316.8	2992.8 ± 786.9
	Winter	1.21 ± 0.12	4.45 ± 0.29	3.04 ± 0.35	1560.4 ± 306.9	1200.9 ± 336.9
	P-value	< 0.001	0.253	< 0.001	0.738	< 0.001
Night	Summer	1.59 ± 0.10	4.46 ± 0.23	3.62 ± 0.26	1602.5 ± 322.1	1418.0 ± 333.1
	Winter	0.64 ± 0.08	3.83 ± 0.27	1.47 ± 0.29	1368.8 ± 274.0	596.3 ± 166.1
	P-value	< 0.001	< 0.001	< 0.001	0.272	< 0.001

extensive impervious surfaces that continuously sustain the heat island effect. The spatial discrepancy between SUHII and SUHIF is further underscored by their weak linear relationships (Fig. 8). As a result, cities with stronger SUHII do not necessarily exhibit higher SUHIF, and vice versa (Figs. 9–10). These discrepancies in SUHII and SUHIF complicate the assessment of the severity of the SUHI effect.

4.3. Performance of SUHIC in characterizing the SUHII effect

SUHIC inherits the advantage of SUHII in highlighting the spatio-temporal variations of the SUHI effect. A significant day-night difference is observed for both the absolute values of annual averages ($SUHIC_A$, 1862.9 ± 500.5 °C km^2 vs. 1046.5 ± 270.2 °C km^2, $p < 0.01$) and the relative values of annual averages ($SUHIC_R$, 4.53 ± 0.51 °C vs. 2.57 ± 0.25 °C, $p < 0.001$) (Table 2). Additionally, SUHIC demonstrates a significant summer-winter difference, with the summertime averages of $SUHIC_A$ and $SUHIC_R$ over European cities being 2–3 times higher than those during wintertime (Table 3). This pronounced diurnal and

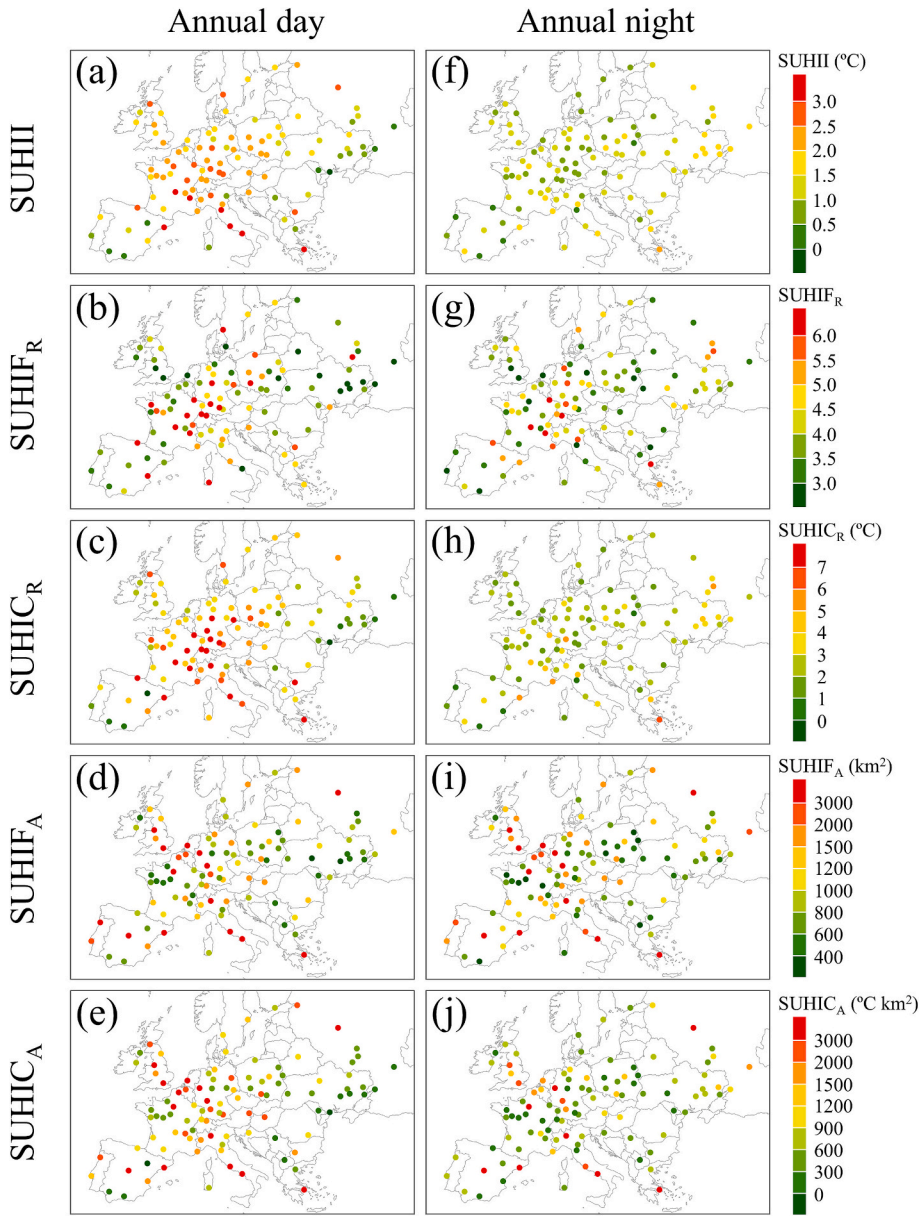

Fig. 7. Spatial variations of SUHII, SUHIF, and SUHIC across 102 European cities. SUHII, SUHIF, and SUHIC denote the intensity, footprint, and capacity of the SUHI effect, respectively. The subscripts A and R indicate the absolute value and relative value of SUHI indicators, respectively.

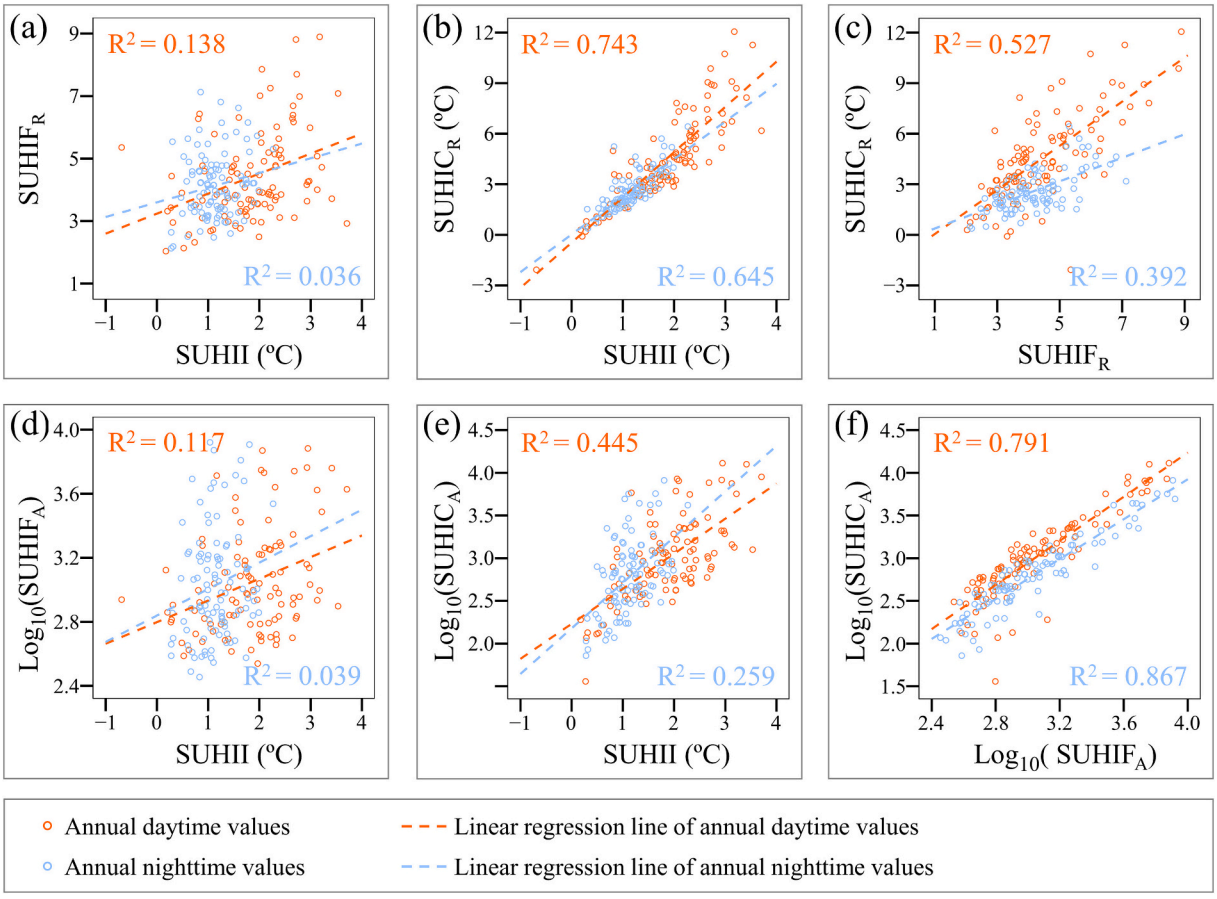

Fig. 8. Associations between SUHII, SUHIF, and SUHIC across 102 European cities. SUHII, SUHIF, and SUHIC represent the intensity, footprint, and capacity of the SUHI effect, respectively. The subscripts A and R refer to the absolute value and relative value of SUHI indicators, respectively.

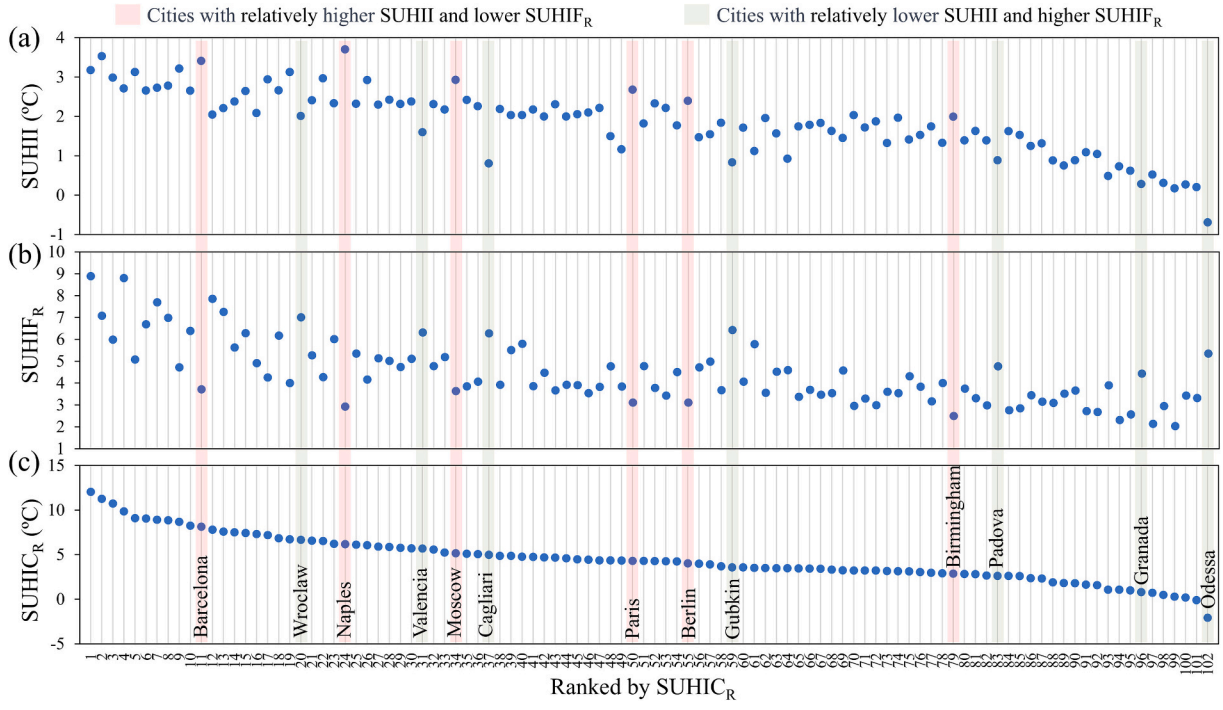

Fig. 9. Variations in rankings of annual daytime SUHI effect for 102 European cities based on different indicators. SUHII, SUHIF, and SUHIC represent the intensity, footprint, and capacity of the SUHI effect, respectively. The subscript R refer to the relative value of SUHI indicators.

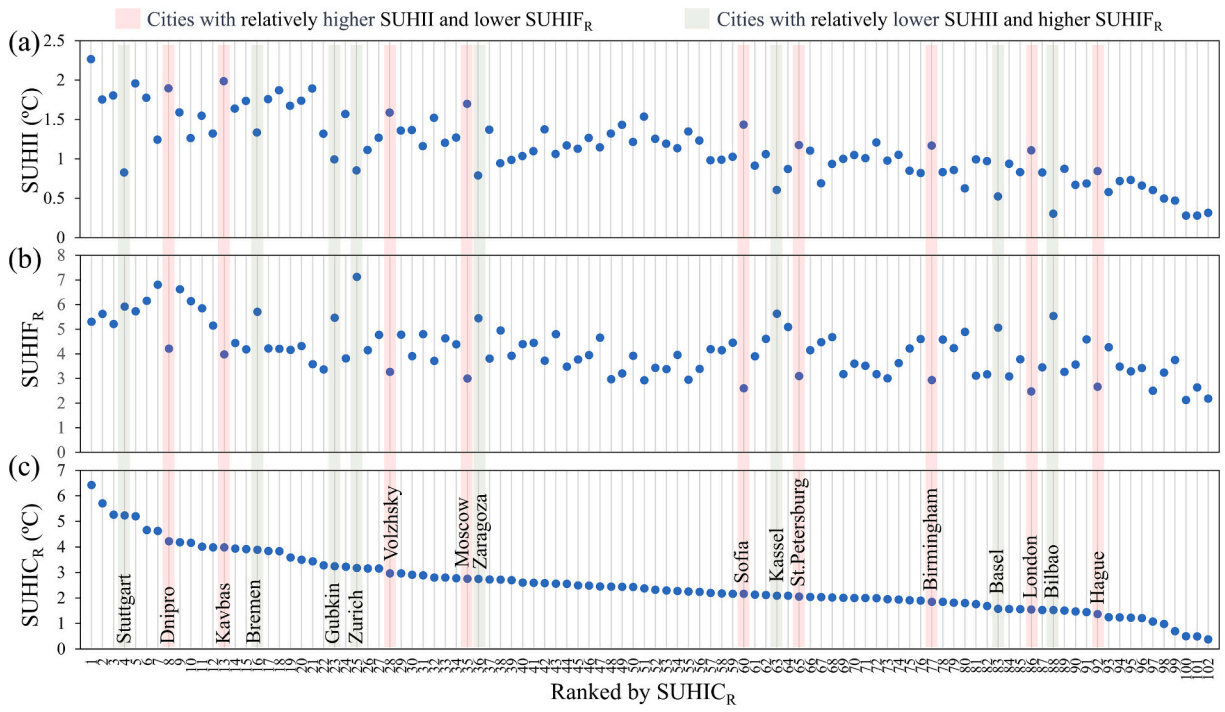

Fig. 10. Same as Fig. 9, but for annual nighttime SUHI effect.

seasonal variability is understandable because SUHIC is a composite indicator that integrates SUHII and SUHIF: with SUHIF remaining relatively stable while SUHII varies substantially, SUHIC ultimately exhibits diurnal and seasonal patterns resembling those of SUHII. In terms of spatial patterns, SUHIC shows strong associations with both SUHII and SUHIF (Fig. 8). Notably, SUHIC demonstrates a significant resemblance to SUHII when considering its relative values ($SUHIC_R$), while more closely matching SUHIF in terms of its absolute values ($SUHIC_A$) (Fig. 7). As a more comprehensive indicator, SUHIC can provide a standard basis for evaluating the SUHI effect in a city when its SUHII and SUHIF diverge (Figs. 9–10).

5. Discussion

5.1. Implications of the SUHIC indicator

Quantifying the SUHI effect is foundational to research on urban thermal environments (Schwarz et al., 2011; Zhou et al., 2018). Numerous SUHI indicators have been proposed, with intensity and footprint being the most typical ones (Zhou et al., 2018). Different indicators vary in terms of their physical definitions and estimation methods, capturing distinct aspects of the SUHI effect (Yang et al., 2023b). Hence, the synergistic combination of multiple indicators aids in providing a more comprehensive evaluation of the SUHI effect (Schwarz et al., 2011). In this context, the SUHIC, which characterizes the SUHI effect from a three-dimensional perspective, provides a valuable supplement to conventional indicators.

It is worth noting that the simultaneous use of multiple indicators can also introduce challenges (Schwarz et al., 2011). When comparing the SUHI effect between cities, discrepancies may emerge because different indicators capture distinct aspects of the phenomenon. As demonstrated in our study, a city may exhibit a high SUHII but a low SUHIF, or vice versa (Figs. 9–10). For instance, Barcelona and Naples display very high SUHII values (> 3.5 °C) but relatively low $SUHIF_R$ (< 4.0) during annual daytime, whereas Cagliari and Gubkin show the opposite pattern, with low SUHII (~1.0 °C) but high $SUHIF_R$ (> 6.0) (Fig. 9). Such inconsistencies complicate evaluation, as it becomes difficult to determine which city experiences a more severe SUHI effect. Furthermore, the weak correlations between SUHII and SUHIF (Fig. 8) also hinder efforts to disentangle the underlying drivers and assess the broader environmental and societal impacts of the SUHI effect (Yang et al., 2023b).

As a composite indicator, the SUHIC integrates both intensity and footprint, thereby providing a more holistic measure of the urban thermal effect. When inconsistencies arise between intensity- and footprint-based evaluations, the SUHIC can serve as a more standardized and reliable indicator (Figs. 9–10), which makes it particularly useful for cross-city comparisons and for linking SUHI characteristics to socio-environmental drivers and impacts.

5.2. Benefits of the DEASE method

(1) The DEASE method demonstrates superior performance in BRA selection

It is well recognized that accurate quantification of the SUHI effect depends on selecting an appropriate BRA (i.e. background reference area) (Chakraborty and Lee, 2019; Li et al., 2018; Li et al., 2022; Schwarz et al., 2011; Yang et al., 2023b; Yao et al., 2024). However, existing methods differ in their BRA selection strategies, introducing substantial uncertainties in SUHI estimation (Liu et al., 2023; Yang et al., 2023b). In this study, we compared the proposed DEASE method with five existing methods (Table 4), including two area-based methods (BRA_{Sub1}, BRA_{Sub2}), two distance-based methods (BRA_{Rur1}, BRA_{Rur2}), and the ASE method.

The BRAs selected by area-based methods are located adjacent to the urban core (Fig. 11), where they may still be influenced by the SUHI effect, leading to systematically lower SUHII estimates compared with other methods (Li et al., 2022; Yang et al., 2023b). In contrast, distance-based methods place BRAs farther from the urban core to reduce the potential urban influence (Yang et al., 2023b). However, because temperature varies markedly along the urban-rural gradient, the mean LST values of BRAs at different distances can differ greatly (Fig. 11a), making BRA selection strategies with fixed-distance unsuitable for cross-city

Table 4
Descriptions of background reference areas (BRAs) extracted by different methods.

Method	BRA name	BRA definition	Reference
Area-based methods	BRA_{Sub1}	The neighboring buffer ring with equal size as the central urban area	Yang et al., 2017; Zhou et al., 2014
	BRA_{Sub2}	The neighboring buffer ring 1.5 times the size of the central urban area	Peng et al., 2012
Distance-based methods	BRA_{Rur1}	The 20 km wide buffer ring located between 10 and 30 km away from the central urban area	Yao et al., 2019
	BRA_{Rur2}	The 5 km wide buffer ring located between 45 and 50 km away from the central urban area	Imhoff et al., 2010
ASE method	BRA_{ASE}	The buffer ring located at the turning point of the urban-rural LST gradients	Yang et al., 2023a

applications (Li et al., 2022). The ASE method can adaptively select BRAs based on urban-rural LST curves, thereby avoiding the arbitrariness of traditional distance-based methods (Yang et al., 2023b). However, the ASE method assumes uniform LST variation outside urban areas and therefore overlooks directional differences in urban-rural LST gradients (Fig. 11b). To address this limitation, our proposed DEASE method adaptively captures the most suitable BRAs in different directions around urban areas (Fig. 11a), thereby improving SUHI estimation, particularly in cities with strong directional difference in urban-rural LST variations (see Section 5.3 for details).

(2) The DEASE method provides a unified framework for the consistent definition and synergistic estimation of multiple SUHI indicators

As previously noted, quantifying the SUHI effect requires consideration of multiple indicators, including the traditional SUHII and SUHIF, as well as the more recently developed SUHIC. These indicators describe different dimensions of the urban thermal environment. Conventional area-based or distance-based methods are generally restricted to measuring the LST difference between urban and rural areas, namely SUHII (Imhoff et al., 2010; Peng et al., 2012; Zhou et al., 2014). Some studies identified that urban temperature profiles approximately follow a Gaussian distribution, and this property has been used to delineate the spatial extents of the SUHI effect, i.e., SUHIF (Streutker, 2003; Yang et al., 2019). More recently, methods based on urban-rural LST gradients have been proposed to jointly quantify SUHII and SUHIF, thus enabling their simultaneous assessment (Yang et al., 2023b; Wang et al., 2024).

Building on above developments, this study proposes the DEASE method, which enables the consistent definition and synergistic estimation of SUHII, SUHIF, and SUHIC. By integrating intensity, footprint, and capacity within a unified framework, the DEASE method provides a more comprehensive representation of the SUHI effect. This integrated approach offers a standardized foundation for cross-city comparisons and long-term monitoring of urban thermal environments.

(3) The DEASE method avoids the restrictions of predefined mathematical models

Based on the assumption that urban LST follow a Gaussian distribution, Yao et al. (2022) employed the Gaussian surface fitting (GSF) method to simultaneously quantify multiple SUHI indicators. However, the GSF method requires urban LST to strictly exhibit a single-peak pattern, which greatly limits its applicability, particularly in polycentric cities (Yang et al., 2023b). As shown in Fig. 12, several European cities contain multiple urban cores, leading to multi-peak LST patterns that deviate markedly from the Gaussian assumption. In such cases, the GSF method fails because its mathematical assumption is not satisfied.

In contrast, the DEASE method imposes no requirement for the urban

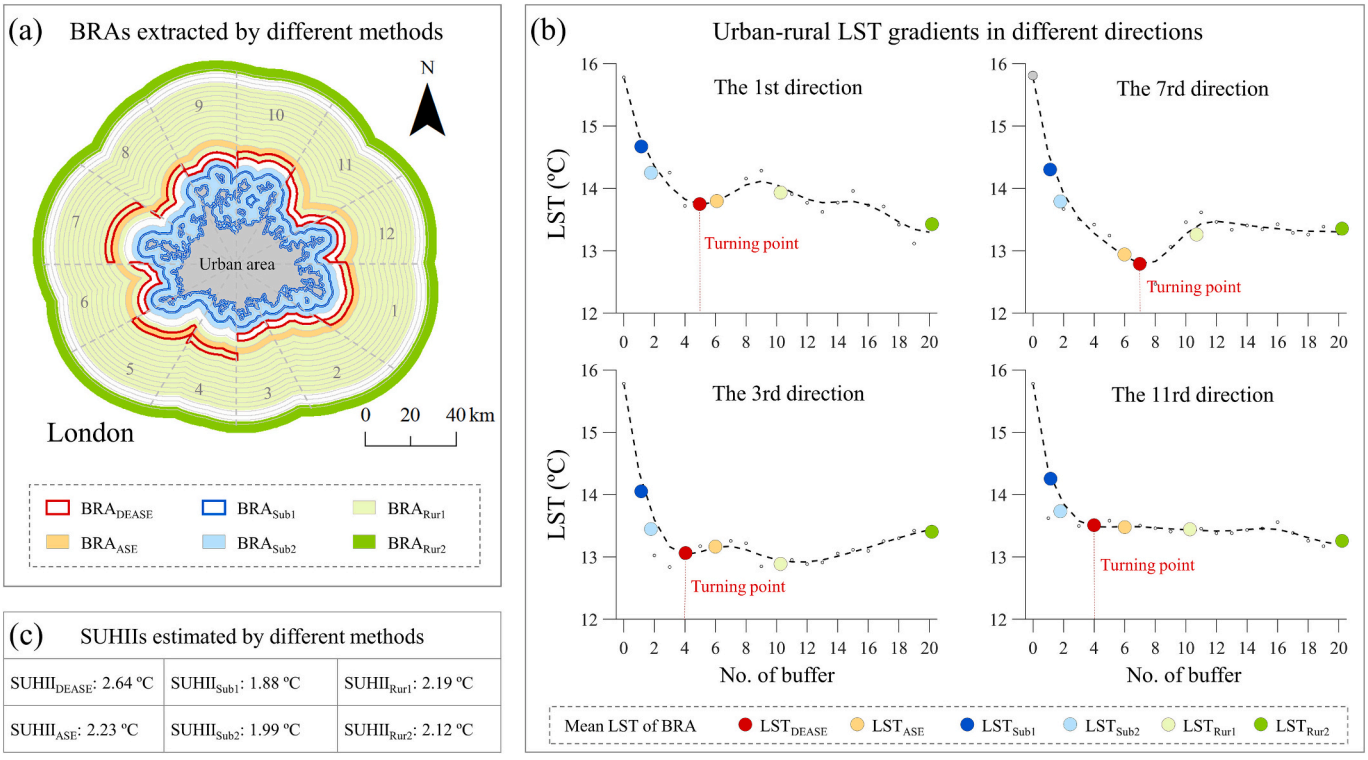

Fig. 11. The background reference areas (BRAs) and SUHI intensity (SUHII) estimates for different methods, using London as an example. (a) The spatial extents of BRAs extracted by different methods. (b) The directional urban-rural LST gradients and the corresponding mean LST of the BRAs. (c) SUHII estimates obtained from different methods. Please refer to Table 4 for details of all the methods.

LST distribution to conform to any predefined mathematical model. Consequently, it is applicable to cities with diverse morphologies, encompassing both monocentric and polycentric structures. Furthermore, the GSF method fundamentally assumes a radially symmetric decay pattern of LST within cities, which results in a symmetric elliptical cross-section in its Gaussian fitting surface (Anniballe et al., 2014). However, urban-rural LST patterns are significantly shaped by land cover heterogeneity and human activities, resulting in marked directional asymmetry (Yang et al., 2023b). These anisotropic variations are challenging to capture using Gaussian-based models but are effectively addressed by our proposed DEASE method (Fig. 12).

In summary, the DEASE method avoids the strict assumptions of parametric models such as the GSF method. This enhances its adaptability and applicability, enabling effective quantification of the SUHI effect in cities with diverse and complex spatial structures.

5.3. Necessity of considering directional variations

Compared to the ASE method developed in our earlier study (Yang et al., 2023b), the DEASE method further advances SUHI quantification by explicitly accounting for directional effects. As depicted in Fig. 13, cities such as Milan, Madrid, and Budapest exhibit marked discrepancies in urban-rural LST gradients across different directions. For these cities, the presence or absence of directional enhancement has a significant impact on the estimated SUHI indicators. Taken Madrid as an example, the SUHII, $SUHIF_R$, and $SUHIC_R$ obtained by the DEASE method are 1.17 °C, 3.85, and 4.34 °C, respectively, which are notably larger than those derived from the ASE method (0.63 °C, 3.58, and 1.45 °C). This demonstrates that neglecting directional differences in urban-rural LST patterns can introduce substantial uncertainty in the quantification of the SUHI effect in some cities.

Such discrepancies are not unexpected, as urban thermal environments are shaped by heterogeneous land cover and human activities, both of which exhibit directional variations (Yang et al., 2023a). For instance, one side of a city may border dense forests or agricultural fields that facilitate cooling, while another side may be adjacent to industrial zones or dense built-up areas that exacerbate heating (Yang et al., 2023a). Consequently, the assumption of radial symmetry, underpinning both the ASE method and many others, oversimplifies the urban thermal landscape and obscures critical directional heterogeneity.

In conclusion, the DEASE method achieves more accurate estimation of SUHI indicators by explicitly accounting for directional variations in urban-rural LST gradients. This makes the DEASE method particularly valuable for use in complex urban environments where asymmetric heat patterns are predominant.

5.4. Sensitivity analysis of the DEASE method

(1) Sensitivity to direction division parameters

As shown in Figs. 14–15, directional division involves two parameters: the division angle and the rotation angle. The division angle determines the number of directions and the size of buffer subdivisions within each direction, while the rotation angle influences the specific orientation of each direction. Changes to these parameters affect how directions are partitioned, which may impact the shape of directional LST curves and the estimated SUHI indicators. To assess their impacts, we compared the estimated values of SUHI indicators obtained under different parameter settings, with the results summarized below.

While adjustments in the division angle and rotation angle result in

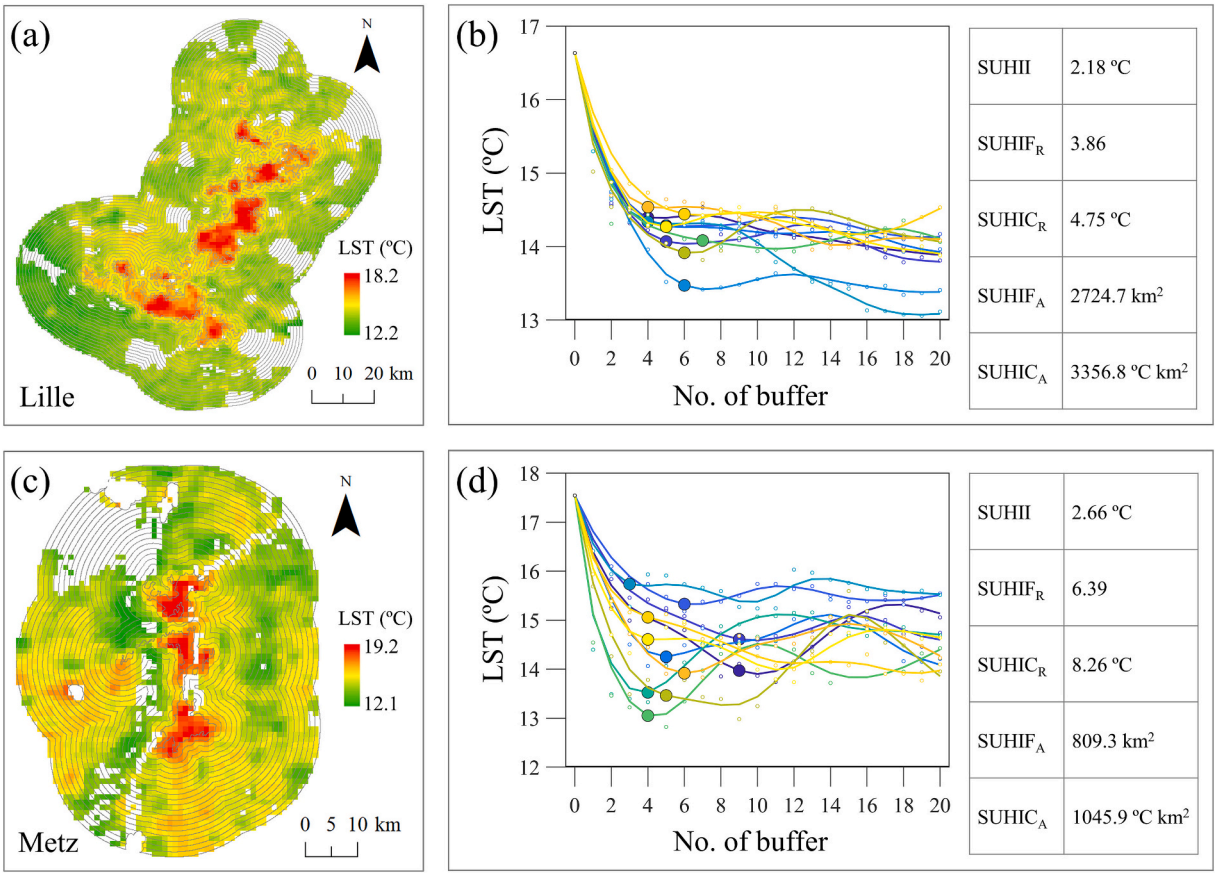

Fig. 12. Examples of LST distributions deviating from the Gaussian model. (a, c) Spatial patterns of annual daytime LST in Lille and Metz. (b, d) Urban-rural LST gradients and the corresponding SUHI indicators estimated by the DEASE method for Lille and Metz.

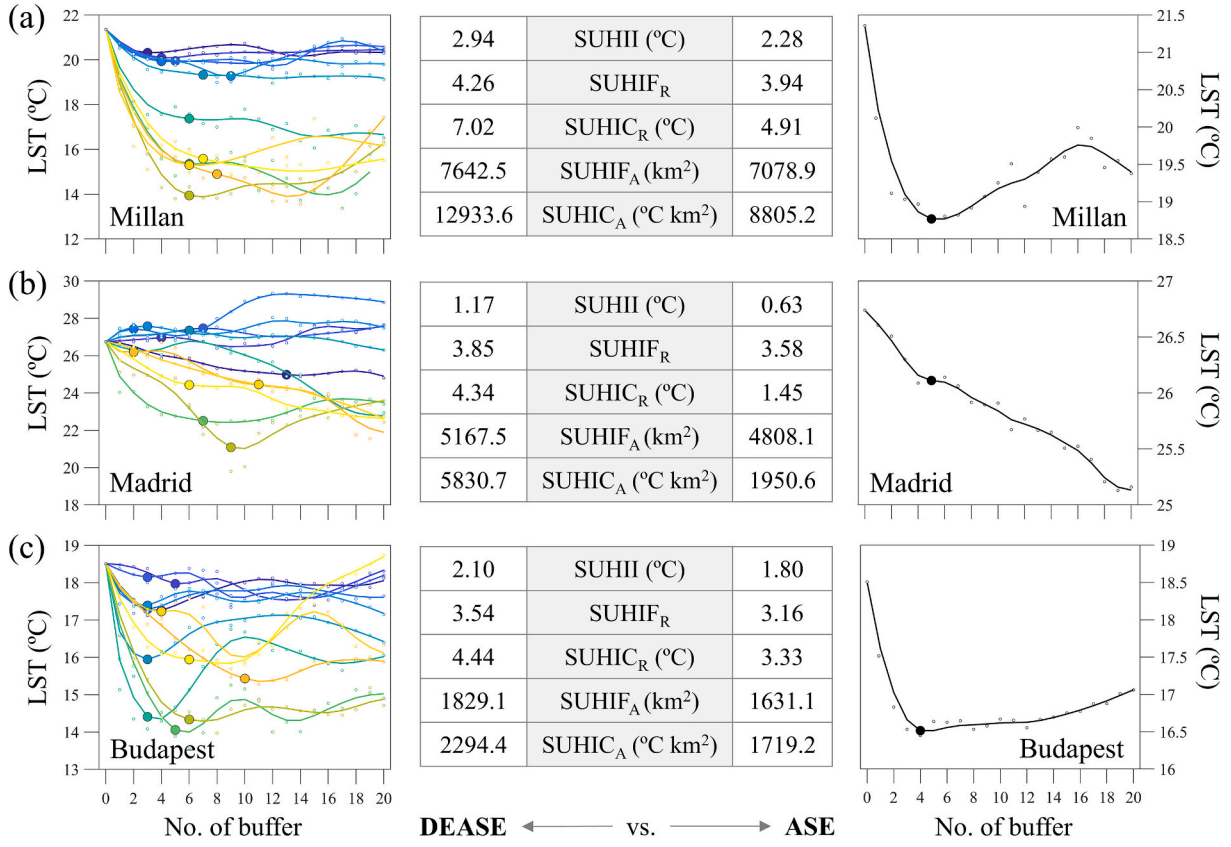

Fig. 13. The influence of directional differences in urban-rural LST variations on quantifying the SUHI effect, taking three typical cities to illustrate. The DEASE method represents a directional refinement of the ASE method, designed to account for the directional variability in urban-rural LST variations when quantifying the SUHI effect.

variations in the SUHI indicator estimates, their overall impacts remain minimal. Typically, transitions in the division angle from 20 degrees to 60 degrees result in variations in SUHII, SUHIF, and SUHIC of less than 3 % for their annual averages (Fig. 14). Likewise, the alterations in SUHII, SUHIF, and SUHIC induced by different values of the rotation angle are also negligible, averaging less than 3 % overall (Fig. 15). This demonstrates, to some extent, the robustness of our proposed DEASE method against variations in direction division parameters.

(2) Sensitivity to LST data errors

The globally seamless LST dataset produced by Zhang et al. (2022) was used in this study because it can avoid the influence of missing data (Mashhoodi and Unceta, 2024; Yang and Zhao, 2023; Yang et al., 2023b; Yuan et al., 2023). Though global validation has demonstrated its relatively good accuracy (RMSE < 2 °C), the errors in LST data may impact the estimated values of SUHI indicators. Since ground-truth values of spatial continuous LST are unavailable, we assessed the potential influence of LST data errors through following simulation experiments.

For each city, we generated simulated error data with the same spatial resolution as the original LST data, setting the RMSE to 2 °C (consistent with the LST data). This simulated error was added to the original LST to create error-containing LST (denoted LST^{err}). Using LST^{err}, we recalculated SUHI indicators (SUHII^{err}, SUHIF^{err}, SUHIC^{err}) for each city with the same methods. We then compared these to the original LST-derived SUHI indicators to evaluate the impact of LST errors. As shown in Fig. 16, LST^{err} exhibits increased spatial noise and local fluctuations along urban-rural gradients compared to the original LST. However, due to the inherent noise resistance of the DEASE method (via spatial smoothing), these noise-induced LST changes had minimal impact on the extraction of the turning points and the estimation of SUHI indicators. As shown in Fig. 17, comparisons across 102 European cities reveal high consistency (near a 1:1 line) between SUHI indicators derived from original LST and LST^{err}. The RMSE between SUHII and SUHII^{err} is approximately 0.2 °C, about 10–20 % of the mean SUHII for all European cities. The impact of LST data errors on SUHIF and SUHIC is even smaller, with RMSEs below 10 % of their respective means. As our simulation assumes errors across all LST pixels, whereas errors in real-world scenarios shall be less widespread, the actual impact of LST data errors is expected to be smaller than that indicated by our simulation experiments. The above analysis underscores the robust noise resistance of the DEASE method and further demonstrates its reliability.

5.5. Limitations and future works

There are still some limitations of this study that need to be addressed by further research. The first issue is about the computational efficiency. Compared with traditional methods, the DEASE method involves obviously higher complexity. For example, quantifying the SUHI effect for a medium-sized city may take several minutes, which could hinder its applicability in large-scale studies to some extent. In the future, efforts can be made to enable its large-scale analysis of the global SUHI effect with the assistance of cloud computing platforms such as Google Earth Engine (Gorelick et al., 2017).

Second, attention should be given to the uncertainties inherent in LST data, including retrieval errors and spatial heterogeneity, which may influence the accuracy of SUHI quantification. Although the proposed DEASE method demonstrates robustness to such uncertainties (Figs. 16–17), their potential impacts cannot be ignored. For example, factors such as complex topography or interference from surrounding urban areas may lead to substantial LST data gaps in certain directions,

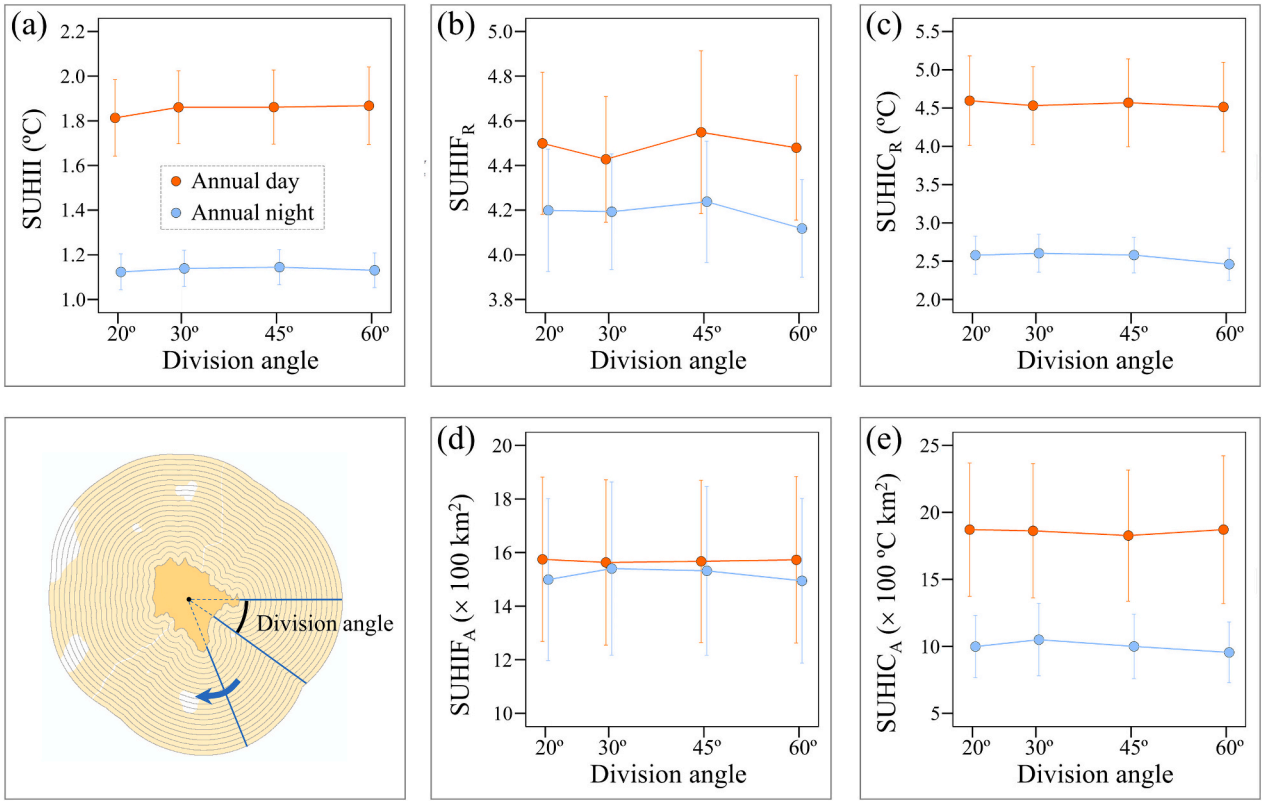

Fig. 14. The sensitivity of SUHI indicators to the division angle parameter of the DEASE method. The division angle determines the number of directions and the size of buffer subdivisions within each direction. SUHII, SUHIF, and SUHIC represent the intensity, footprint, and capacity of the SUHI effect, respectively. The subscripts A and R refer to the absolute value and relative value of SUHI indicators, respectively.

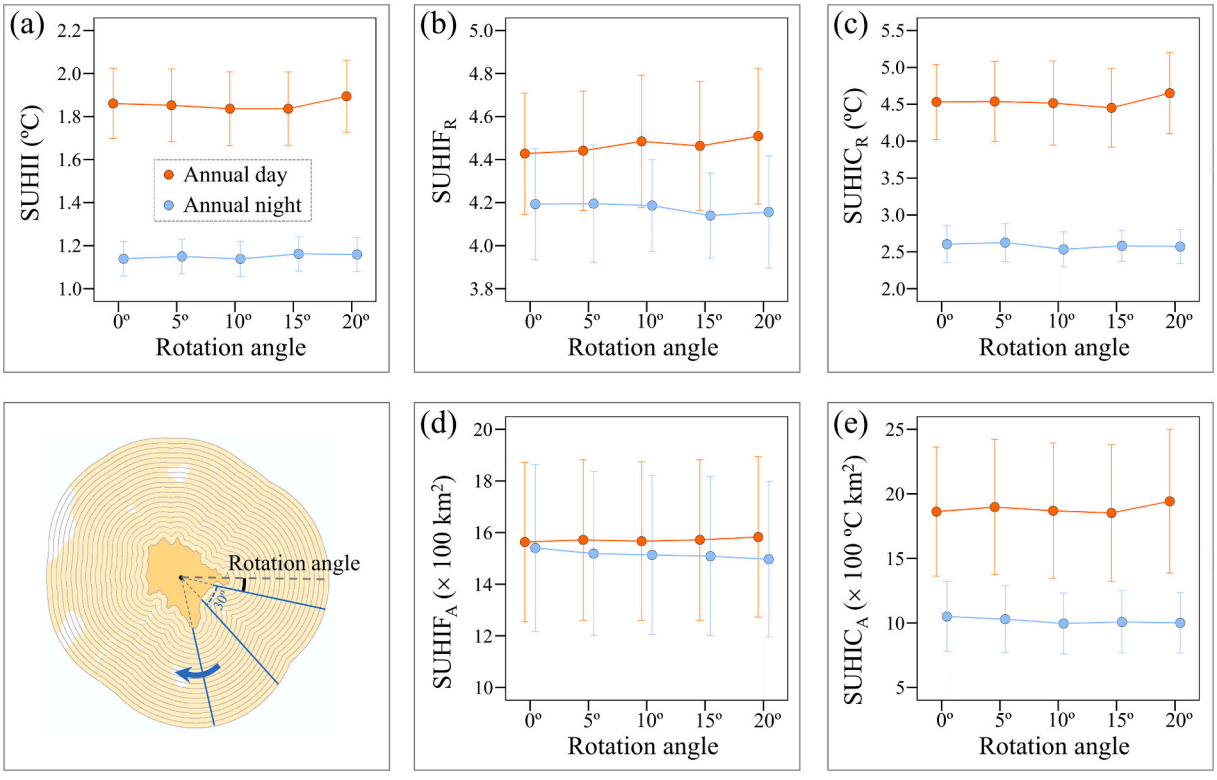

Fig. 15. The sensitivity of SUHI indicators to the rotation angle parameter of the DEASE method. The rotation angle influences the specific orientation of each direction. SUHII, SUHIF, and SUHIC represent the intensity, footprint, and capacity of the SUHI effect, respectively. The subscripts A and R refer to the absolute value and relative value of SUHI indicators, respectively.

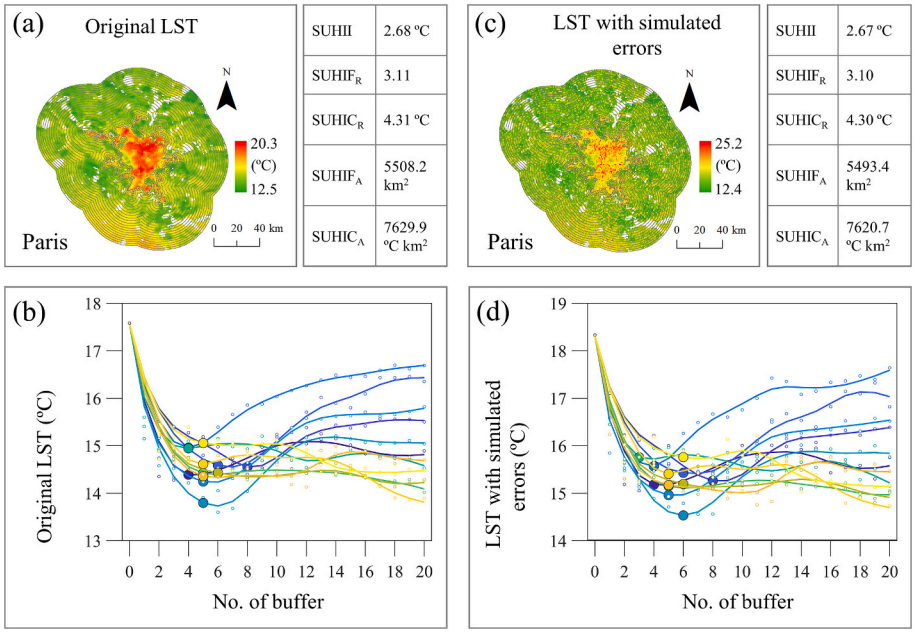

Fig. 16. The influence of LST data errors on the quantification of the SUHI effect, using Paris as an example. (a-b) The original LST and the corresponding estimated SUHI indicator values. (c-d) The LST with simulated errors (LST^{err}) and the corresponding estimated SUHI indicator values. The LST^{err} is derived by adding simulated random errors (RMSE = 2 °C) to the original LST. SUHII, SUHIF, and SUHIC represent the intensity, footprint, and capacity of the SUHI effect, respectively. The subscripts "A" and "R" refer to the absolute value and relative values of the SUHI indicators, respectively. The superscript "err" denotes the SUHI indicators estimated using the LST^{err}.

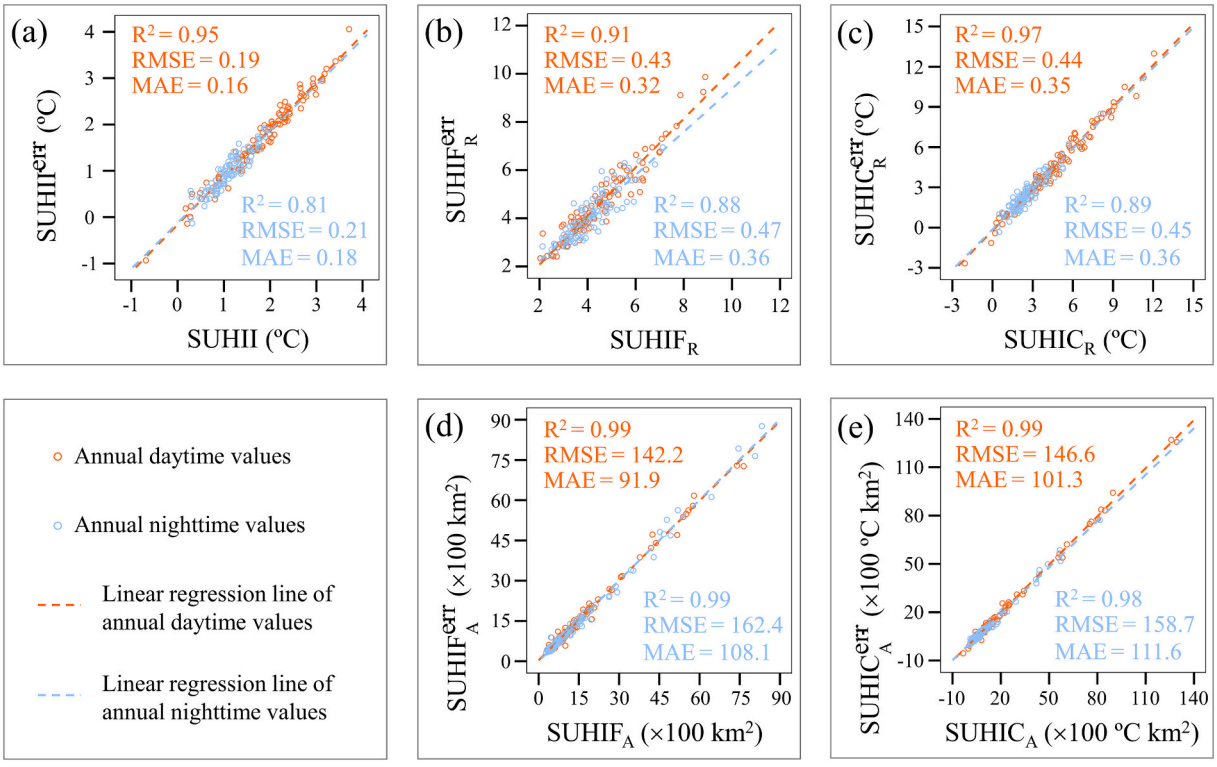

Fig. 17. The comparisons between the SUHI indicators estimated using the original LST and those estimated using the LST with simulated errors (LST^{err}). The LST^{err} is derived by adding simulated random errors (RMSE = 2 °C) to the original LST. SUHII, SUHIF, and SUHIC represent the intensity, footprint, and capacity of the SUHI effect, respectively. The subscripts "A" and "R" refer to the absolute value and relative values of the SUHI indicators, respectively. The superscript "err" denotes the SUHI indicators estimated using the LST^{err}.

making it challenging to reliably identify the turning point along urban-rural LST gradients. These challenges are further exacerbated in densely urbanized regions due to the prevalence of clustered cities and intricate urban morphologies. The resulting LST data gaps amplify directional uncertainty and compromise the interpretation of urban-rural LST gradients. In such cases, missing values are replaced with mean LST values from other directions; however, such substitution may introduce bias in SUHI estimation, particularly in cities with strong directional differences in urban-rural LST gradients. Future work should place greater emphasis on evaluating and correcting such uncertainties to improve the reliability and generalizability of the framework.

Third, while this study provides preliminary theoretical and experimental evidence of the benefits of the DEASE method and the SUHIC indicator, there remains a need for a more comprehensive examination of their application potential in future research. For example, the SUHIC indicator could be utilized to analyze the spatiotemporal variations of the SUHI effect and underlying driving factors by integrating large-scale, long time-series, and multi-source remote sensing data. Building upon this foundation, a more thorough assessment of SUHIC could be achieved by comparing and analyzing it alongside existing research findings. Furthermore, since air temperature UHI (AUHI) is more relevant to urbanization-induced local heat exposure than SUHI, with air temperature generally showing somewhat distinct distributions from those for LST (Chakraborty et al., 2022), it is worth investigating whether the DEASE method can be extended to quantify AUHI. This may involve shifting from an area-normalized to a population-normalized framework to better capture impacts on human thermal exposure.

Finally, the DEASE method and the SUHIC indicator introduced in this study are suitable for quantitatively assessing the SUHI effect at the city scale. While this city-scale analysis aids in understanding the overall impact of urbanization on the thermal environment, it lacks a detailed assessment of the fine distribution of the SUHI effect within urban areas. This fine-scale analysis is essential for understanding urban environmental equity and guiding urban planning decisions (Chakraborty et al., 2023; Chang et al., 2021; Hsu et al., 2021). Future studies should therefore aim to refine the framework for fine-scale applications and develop new indicators tailored to neighborhood- or district-level thermal environment analysis.

6. Conclusion

Research on urban thermal dynamics has focused on the SUHI effect, yet accurately measuring it with remotely sensed LST remains challenging. This study is concentrated on the development of improved methods for quantifying the SUHI effect, with key innovations and findings summarized as follows:

(1) To more comprehensively quantify the SUHI effect, this study introduces the SUHI capacity (SUHIC) indicator, which addresses the limitations of conventional indicators (SUHII and SUHIF) that characterize the SUHI effect only from a peak perspective, by incorporating cumulative thermal signals from both urban and surrounding areas. When assessing the SUHI effect, especially in cases where SUHII and SUHIF conflicts, SUHIC serves as a more holistic indicator and provides critical reference value. It can therefore be regarded as a valuable supplement to the existing SUHI indicator system.

(2) Considering the directional differences in LST changes from urban to rural areas, this study proposes a DEASE method that simultaneously quantifies the effects of SUHII, SUHIF and SUHIC, without requiring predefined mathematical model. Experimental results demonstrate that considering directional differences can affect the estimated SUHI indicators, particularly in cities with substantial directional variations in urban-rural LST gradients. This highlights the crucial importance of our DEASE method, which incorporates directional enhancement.

(3) The analysis of 102 European cities reveals that SUHII displays significant diurnal and seasonal variations, while SUHIF remains consistent across different periods. Interestingly, absolute values of SUHIC exhibit similarities to those of SUHIF, while its relative values (normalized by the urban area) show a closer alignment with SUHII. Moreover, SUHIC exhibits strong diurnal and seasonal variability in both absolute and relative values, thereby inheriting the advantage of SUHII in highlighting the spatiotemporal variations of the SUHI effect.

In summary, this study proposes a novel DEASE method for quantifying the SUHI effect by accounting for directional differences in urban-rural LST gradients. This approach enables estimation of both conventional indicators (SUHII and SUHIF) and a composite indicator, SUHIC, which captures cumulative thermal signals from urbanization for a more comprehensive assessment. The proposed method and indicator provide valuable tools for evaluating the urban thermal environment.

CRediT authorship contribution statement

Qiquan Yang: Writing – review & editing, Writing – original draft, Software, Methodology, Funding acquisition, Conceptualization. **Richen Ye:** Writing – review & editing, Resources, Formal analysis. **TC Chakraborty:** Writing – review & editing, Visualization. **Ting Hu:** Writing – review & editing, Writing – original draft, Software, Validation, Conceptualization. **Yue Liu:** Writing – review & editing, Writing – original draft, Software, Investigation, Conceptualization.

Declaration of competing interest

The authors declare that they have no known competing financial interests or personal relationships that could have appeared to influence the work reported in this paper.

Acknowledgment

This research was supported by the National Natural Science Foundation of China (42201389, 42201377). TC's contribution was supported by a U.S. Department of Energy Office of Science Early Career grant. PNNL is operated for the Department of Energy by Battelle Memorial Institute under contract DE-AC05-76RL01830.

Data availability

The global urban boundary (GUB) dataset can be freely available from http://data.starcloud.pcl.ac.cn/zh/resource/14. The seamless LST products can be publicly downloaded from https://iastate.figshare.com/collections/A_global_seamless_1_km_resolution_daily_land_surface_temperature_dataset_2003_2020_/5078492. The Köppen-Geiger climate classification map is available from https://www.gloh2o.org/koppen/. All the other data can be accessed from the Google Earth Engine platform (https://code.earthengine.google.com/). All data are available upon reasonable request from the authors.

References

Anniballe, R., Bonafoni, S., Pichierri, M., 2014. Spatial and temporal trends of the surface and air heat island over Milan using MODIS data. Remote Sens. Environ. 150, 163–171.

Beck, H.E., Zimmermann, N.E., McVicar, T.R., Vergopolan, N., Berg, A., Wood, E.F., 2018. Present and future Köppen-Geiger climate classification maps at 1-km resolution. Sci Data 5, 1–12.

Chakraborty, T., Lee, X., 2019. A simplified urban-extent algorithm to characterize surface urban heat islands on a global scale and examine vegetation control on their spatiotemporal variability. Int. J. Appl. Earth Obs. Geoinf. 74, 269–280.

Chakraborty, T., Hsu, A., Manya, D., Sheriff, G., 2020. A spatially explicit surface urban heat island database for the United States: characterization, uncertainties, and possible applications. ISPRS J. Photogramm. Remote Sens. 168, 74–88.

Chakraborty, T., Venter, Z.S., Qian, Y., Lee, X., 2022. Lower urban humidity moderates outdoor heat stress. AGU Adv. 3, e2022AV000729.
Chakraborty, T., Newman, A.J., Qian, Y., Hsu, A., Sheriff, G., 2023. Residential segregation and outdoor urban moist heat stress disparities in the United States. One Earth 6, 738–750.
Chang, Y., Xiao, J., Li, X., Middel, A., Zhang, Y., Gu, Z., Wu, Y., He, S., 2021. Exploring diurnal thermal variations in urban local climate zones with ECOSTRESS land surface temperature data. Remote Sens. Environ. 263, 112544.
Chang, Y., Xiao, J., Li, X., Weng, Q., 2023. Monitoring diurnal dynamics of surface urban heat island for urban agglomerations using ECOSTRESS land surface temperature observations. Sustain. Cities Soc. 98, 104833.
Chang, Y., Weng, Q., Voogt, J.A., Xiao, J., 2025. Urban thermal anisotropies by local climate zones: an assessment using multi-angle land surface temperatures from ECOSTRESS. Remote Sens. Environ. 322, 114705.
Deng, X., Yu, W., Shi, J., Huang, Y., Li, D., He, X., Zhou, W., Xie, Z., 2024. Characteristics of surface urban heat islands in global cities of different scales: trends and drivers. Sustain. Cities Soc. 107, 105483.
Du, H., Zhan, W., Voogt, J., Bechtel, B., Chakraborty, T.C., Liu, Z., Hu, L., Wang, Z., Li, J., Fu, P., 2023. Contrasting trends and drivers of global surface and canopy urban heat islands. Geophys. Res. Lett. 50, e2023GL104661.
García-León, D., Casanueva, A., Standardi, G., Burgstall, A., Flouris, A.D., Nybo, L., 2021. Current and projected regional economic impacts of heatwaves in Europe. Nat. Commun. 12 (1), 5807.
Gorelick, N., Hancher, M., Dixon, M., Ilyushchenko, S., Thau, D., Moore, R., 2017. Google earth engine: planetary-scale geospatial analysis for everyone. Remote Sens. Environ. 202, 18–27.
Guo, X., Du, H., Zhan, W., Ji, Y., Wang, C., Wang, C., Ge, S., Wang, S., Li, J., Jiang, S., 2025. Global patterns and determinants of year-to-year variations in surface urban heat islands. ISPRS J. Photogramm. Remote Sens. 223, 399–412.
Hsu, A., Sheriff, G., Chakraborty, T., Manya, D., 2021. Disproportionate exposure to urban heat island intensity across major US cities. Nat. Commun. 12, 2721.
Imhoff, L., Zhang, P., Wolfe, E., Bounoua, L., 2010. Remote sensing of the urban heat island effect across biomes in the continental USA. Remote Sens. Environ. 114, 504–513.
Lai, J., Zhan, W., Huang, F., Quan, J., Hu, L., Gao, L., Ju, W., 2018. Does quality control matter? Surface urban heat island intensity variations estimated by satellite-derived land surface temperature products. ISPRS J. Photogramm. Remote Sens. 139, 212–227.
Lai, J., Zhan, W., Voogt, J., Quan, J., Huang, F., Zhou, J., Bechtel, B., Hu, L., Wang, K., Cao, C., 2021. Meteorological controls on daily variations of nighttime surface urban heat islands. Remote Sens. Environ. 253, 112198.
Li, H., Zhou, Y., Li, X., Meng, L., Wang, X., Wu, S., Sodoudi, S., 2018. A new method to quantify surface urban heat island intensity. Sci. Total Environ. 624, 262–272.
Li, K., Chen, Y., Wang, M., Gong, A., 2019. Spatial-temporal variations of surface urban heat island intensity induced by different definitions of rural extents in China. Sci. Total Environ. 669, 229–247.
Li, X., Gong, P., Zhou, Y., Wang, J., Bai, Y., Chen, B., Hu, T., Xiao, Y., Xu, B., Yang, J., 2020. Mapping global urban boundaries from the global artificial impervious area (GAIA) data. Environ. Res. Lett. 15, 094044.
Li, K., Chen, Y., Gao, S., 2022. Uncertainty of city-based urban heat island intensity across 1112 global cities: background reference and cloud coverage. Remote Sens. Environ. 271, 112898.
Li, L., Zhan, W., Hu, L., Chakraborty, T., Wang, Z., Fu, P., Wang, D., Liao, W., Huang, F., Fu, H., 2023. Divergent urbanization-induced impacts on global surface urban heat island trends since 1980s. Remote Sens. Environ. 295, 113650.
Liu, Z., Zhan, W., Bechtel, B., Voogt, J., Lai, J., Chakraborty, T., Wang, Z.-H., Li, M., Huang, F., Lee, X., 2022. Surface warming in global cities is substantially more rapid than in rural background areas. Commun. Earth Environ. 3, 219.
Liu, H., He, B.-J., Gao, S., Zhan, Q., Yang, C., 2023. Influence of non-urban reference delineation on trend estimate of surface urban heat island intensity: a comparison of seven methods. Remote Sens. Environ. 296, 113735.
Mashhoodi, B., Unceta, P.M., 2024. Urban form and surface temperature inequality in 683 European cities. Sustain. Cities Soc. 113, 105690.
Pekel, J.-F., Cottam, A., Gorelick, N., Belward, A.S., 2016. High-resolution mapping of global surface water and its long-term changes. Nature 540, 418–422.
Peng, S., Piao, S., Ciais, P., Friedlingstein, P., Ottle, C., Bréon, F.-M., Nan, H., Zhou, L., Myneni, R.B., 2012. Surface urban heat island across 419 global big cities. Environ. Sci. Technol. 46, 696–703.
Rajagopal, P., Priya, R.S., Senthil, R., 2023. A review of recent developments in the impact of environmental measures on urban heat island. Sustain. Cities Soc. 88, 104279.
Rizwan, A.M., Dennis, L.Y., Chunho, L., 2008. A review on the generation, determination and mitigation of urban Heat Island. J. Environ. Sci. 20, 120–128.
Schwarz, N., Lautenbach, S., Seppelt, R., 2011. Exploring indicators for quantifying surface urban heat islands of European cities with MODIS land surface temperatures. Remote Sens. Environ. 115, 3175–3186.
Shreevastava, A., Prasanth, S., Ramamurthy, P., Rao, P.S.C., 2021. Scale-dependent response of the urban heat island to the European heatwave of 2018. Environ. Res. Lett. 16 (10), 104021.
Si, M., Li, Z.-L., Nerry, F., Tang, B.-H., Leng, P., Wu, H., Zhang, X., Shang, G., 2022. Spatiotemporal pattern and long-term trend of global surface urban heat islands characterized by dynamic urban-extent method and MODIS data. ISPRS J. Photogramm. Remote Sens. 183, 321–335.
Streutker, D.R., 2003. Satellite-measured growth of the urban heat island of Houston, Texas. Remote Sens. Environ. 85, 282–289.
Van, Z., Jakob, J., 2001. The shuttle radar topography Mission (SRTM): a breakthrough in remote sensing of topography. Acta Astronaut. 48 (5–12), 559–565.
Voogt, J.A., Oke, T.R., 2003. Thermal remote sensing of urban climates. Remote Sens. Environ. 86, 370–384.
Wang, Y., Wang, H., Yao, F., Stouffs, R., Wu, J., 2024. An integrated framework for jointly assessing spatiotemporal dynamics of surface urban heat island intensity and footprint: China, 2003–2020. Sustain. Cities Soc. 112, 105601.
Wang, S., Zhan, W., Zhou, B., Tong, S., Chakraborty, T.C., Wang, Z., Huang, K., Du, H., Middel, A., Li, J., 2025. Dual impact of global urban overheating on mortality. Nat. Clim. Chang. 1–8.
Weng, Q., 2009. Thermal infrared remote sensing for urban climate and environmental studies: methods, applications, and trends. ISPRS J. Photogramm. Remote Sens. 64, 335–344.
Wong, N.H., Tan, C.L., Kolokotsa, D.D., Takebayashi, H., 2021. Greenery as a mitigation and adaptation strategy to urban heat. Nat. Rev. Earth Environ. 2, 166–181.
Yang, C., Zhao, S., 2023. Diverse seasonal hysteresis of surface urban heat islands across Chinese cities: patterns and drivers. Remote Sens. Environ. 294, 113644.
Yang, Q., Huang, X., Li, J., 2017. Assessing the relationship between surface urban heat islands and landscape patterns across climatic zones in China. Sci. Rep. 7, 9337–9347.
Yang, Q., Huang, X., Tang, Q., 2019. The footprint of urban heat island effect in 302 Chinese cities: temporal trends and associated factors. Sci. Total Environ. 655, 652–662.
Yang, K., Tao, F., Wang, C.-L., Wang, Z.-L., Han, Q.-L., Zhou, T., 2023a. An optimization method for surface urban heat island footprint extraction based on anisotropy assumption. Urban Clim. 49, 101532.
Yang, Q., Xu, Y., Tong, X., Huang, X., Liu, Y., Chakraborty, T.C., Xiao, C., Hu, T., 2023b. An adaptive synchronous extraction (ASE) method for estimating intensity and footprint of surface urban heat islands: a case study of 254 north American cities. Remote Sens. Environ. 297, 113777.
Yao, R., Wang, L., Huang, X., Niu, Y., Chen, Y., Niu, Z., 2018. The influence of different data and method on estimating the surface urban heat island intensity. Ecol. Indic. 89, 45–55.
Yao, R., Wang, L., Huang, X., Gong, W., Xia, X., 2019. Greening in rural areas increases the surface urban heat island intensity. Geophys. Res. Lett. 46, 2204–2212.
Yao, L., Sun, S., Song, C., Wang, Y., Xu, Y., 2022. Recognizing surface urban heat 'island'effect and its urbanization association in terms of intensity, footprint, and capacity: a case study with multi-dimensional analysis in northern China. J. Clean. Prod. 372, 133720.
Yao, R., Huang, X., Zhang, Y., Wang, L., Li, J., Yang, Q., 2024. Estimation of the surface urban heat island intensity across 1031 global cities using the regression-modification-estimation (RME) method. J. Clean. Prod. 434, 140231.
Yuan, B., Li, X., Zhou, L., Bai, T., Hu, T., Huang, J., Liu, D., Li, Y., Guo, J., 2023. Global distinct variations of surface urban heat islands in inter-and intra-cities revealed by local climate zones and seamless daily land surface temperature data. ISPRS J. Photogramm. Remote Sens. 204, 1–14.
Zhang, T., Zhou, Y., Zhu, Z., Li, X., Asrar, G.R., 2022. A global seamless 1 km resolution daily land surface temperature dataset (2003–2020). Earth Syst. Sci. Data 14, 651–664.
Zhou, D., Zhao, S., Liu, S., Zhang, L., Zhu, C., 2014. Surface urban heat island in China's 32 major cities: spatial patterns and drivers. Remote Sens. Environ. 152, 51–61.
Zhou, D., Zhao, S., Zhang, L., Sun, G., Liu, Y., 2015. The footprint of urban heat island effect in China. Sci. Rep. 5, 11160.
Zhou, D., Xiao, J., Bonafoni, S., Berger, C., Deilami, K., Zhou, Y., Frolking, S., Yao, R., Qiao, Z., Sobrino, J.A., 2018. Satellite remote sensing of surface urban heat islands: progress, challenges, and perspectives. Remote Sens 11, 48.
Zhou, D., Xiao, J., Frolking, S., Zhang, L., Zhou, G., 2022. Urbanization contributes little to global warming but substantially intensifies local and regional land surface warming. Earth's Future 10, e2021EF002401.